PLOS BIOLOGY

RESEARCH ARTICLE

Coordinated circadian timing through the integration of local inputs in *Arabidopsis thaliana*

Mark Greenwood[1,2], **Mirela Domijan**[3], **Peter D. Gould**[4], **Anthony J. W. Hall**[5], **James C. W. Locke**[1,6]*

1 Sainsbury Laboratory, University of Cambridge, Cambridge, United Kingdom, **2** Department of Biochemistry, University of Cambridge, Cambridge, United Kingdom, **3** Department of Mathematical Sciences, University of Liverpool, Liverpool, United Kingdom, **4** Institute of Integrative Biology, University of Liverpool, Liverpool, United Kingdom, **5** Earlham Institute, Norwich, United Kingdom, **6** Microsoft Research, Cambridge, United Kingdom

* james.locke@slcu.cam.ac.uk

Citation: Greenwood M, Domijan M, Gould PD, Hall AJW, Locke JCW (2019) Coordinated circadian timing through the integration of local inputs in *Arabidopsis thaliana*. PLoS Biol 17(8): e3000407. https://doi.org/10.1371/journal.pbio.3000407

Academic Editor: Mark Estelle, UCSD, UNITED STATES

Received: March 15, 2019

Accepted: July 11, 2019

Published: August 15, 2019

Data Availability Statement: Underlying quantitative data and model code are available from the project GitLab page (www.gitlab.com/slcu/teamJL/greenwood_etal_2019).

Funding: MG and JCWL were funded by the Gatsby Foundation (www.gatsby.org.uk; GAT3395/GLC). JCWL and MD were funded by the Biotechnology and Biological Sciences Research Council (www.bbsrc.ukri.org; BB/K017152/1). PDG and AJWH were funded by the Biotechnology and Biological Sciences Research Council (www.bbsrc.

Abstract

Individual plant cells have a genetic circuit, the circadian clock, that times key processes to the day-night cycle. These clocks are aligned to the day-night cycle by multiple environmental signals that vary across the plant. How does the plant integrate clock rhythms, both within and between organs, to ensure coordinated timing? To address this question, we examined the clock at the sub-tissue level across *Arabidopsis thaliana* seedlings under multiple environmental conditions and genetic backgrounds. Our results show that the clock runs at different speeds (periods) in each organ, which causes the clock to peak at different times across the plant in both constant environmental conditions and light-dark (LD) cycles. Closer examination reveals that spatial waves of clock gene expression propagate both within and between organs. Using a combination of modeling and experiment, we reveal that these spatial waves are the result of the period differences between organs and local coupling, rather than long-distance signaling. With further experiments we show that the endogenous period differences, and thus the spatial waves, can be generated by the organ specificity of inputs into the clock. We demonstrate this by modulating periods using light and metabolic signals, as well as with genetic perturbations. Our results reveal that plant clocks can be set locally by organ-specific inputs but coordinated globally via spatial waves of clock gene expression.

Introduction

In response to the Earth's predictable light-dark (LD) cycles, many organisms have evolved a circadian clock [1]. A common design principle is a central oscillator that receives input from multiple environmental signals and uses them to predict the time of day. This timing information is used to coordinate processes, matching them to the optimum time of day or year. In plants, these processes include photosynthesis, leaf movement, and flowering [2].

A number of studies have reported that different parts of the plant can generate circadian oscillations with different periods under constant conditions [3]. This could be due to the

ukri.org; BB/K018078/1). The funders had no role in study design, data collection and analysis, decision to publish, or preparation of the manuscript.

Competing interests: The authors have declared that no competing interests exist.

Abbreviations: DCMU, 3-(3,4-dichlorophenyl)-1,1-dimethylurea; DD, constant darkness; *ELF4*, *EARLY FLOWERING 4*; FFT-NLLS, fast Fourier transformed nonlinear least squares; *GI*, *GIGANTEA*; LD, light-dark; LL, constant light; *LUC*, *LUCIFERASE*; MS, Murashige and Skoog; *PHYB*, *PHYTOCHROME B*; *PRR9*, *PSEUDO-RESPONSE REGULATOR 9*; ROI, region of interest; SCN, suprachiasmatic nucleus; *TOC1*, *TIMING OF CAB EXPRESSION 1*.

clock network being wired differently in different parts of the plant, or that the sensitivity of the clock to environmental inputs varies across the plant. There is already some evidence that both the network and inputs have some cell or tissue specificity. Previous work has shown that although most clock genes are expressed in most cell types [4–7], some core clock genes have a tissue-enriched expression pattern [4,8–10]. Mutations to some core clock genes may also have differential effects on the root and shoot [9]. Additionally, it has been shown that clocks in different cell types respond preferentially to temperature or light inputs [11–13], and that the shoot and root clocks have different sensitivities to light [6]. However, how whole-plant timing is affected by tissue-level differences in the clock network or differences in sensitivity to clock inputs remains unclear.

In complex organisms, many physiological processes, including those under control of the clock, require coordinated timing across tissues. In many eukaryotes, cell-cell communication maintains clock coherence across the organism. For example, in mammals, clock cells located in the suprachiasmatic nucleus (SCN) drive rhythms in peripheral tissues across the body via neural and humoral signals [1,14]. Peripheral tissues have the same clock network as in the SCN [15,16], although the relative importance of each circuit component may vary between tissues [17]. In plants, studies of synchronization [5,18–23], grafting experiments [22], and the use of tissue-specific promoters [10] suggest that cell-cell communication is also important for coherent rhythms. It has been proposed that this communication acts hierarchically, with the root clock dependent on a signal from the shoot [9,22,24]. However, a decentralized structure, with multiple points of coordination across the plant, could potentially explain inconsistencies such as fast cells in the root tip [5], spiral and striped expression patterns in leaves and roots [18–20,25–27], and the entrainment of detached roots by light [6,28]. Therefore, how plants coordinate the clock at the organism level is not understood (Fig 1).

Plant cells can communicate locally with their neighbors via the diffusion of molecules through the cell wall, or through microscopic channels called plasmodesmata [29]. Longer-distance communication is also possible through molecules being selectively loaded into the phloem translocation stream. Both local and long-distance mechanisms have been proposed to coordinate circadian rhythms in plants [5,18–24]. However, the relative importance of local versus long-distance communication for the whole-organism coordination of rhythms has not been resolved.

In this work, we examined the clock at the sub-tissue level across *A. thaliana* seedlings in vivo. We observed that each organ of the plant has a different clock phase, even under LD cycles. Sub-tissue–level analysis revealed that spatial waves of clock gene expression propagate within and between the organs. Mathematical models propose that waves under both constant light (LL) and LD cycles could be due to the combination of different periods in each part of the plant and local cell-cell coupling. We tested these predictions by examining rhythms in dissected plant roots. Waves up and down the root persisted in detached roots, showing that long-distance signals from the shoot are not required for coordination. Next, by modulating periods in specific parts of the plant using genetic and environmental perturbations, we found that we could alter wave generation in a predictable manner. Thus, the clock in plants has a decentralized structure, with clocks across the plant coordinating via local cell-cell signaling.

Results

Organ-specific clocks entrain to LD cycles with different phases

To investigate the coordination of clock rhythms, we analyzed rhythms across entire seedlings under different entrainment regimes. To do this, we monitored promoter activity of the core clock gene *GIGANTEA* (*GI*) [30] fused to the *LUCIFERASE* (*LUC*) reporter gene, for multiple

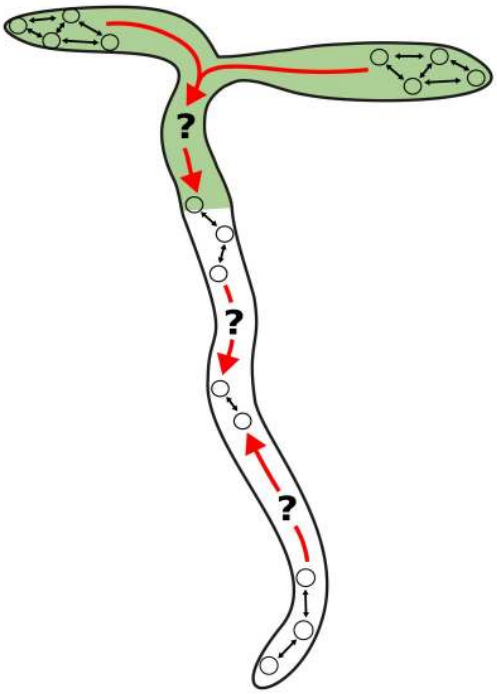

Fig 1. How do circadian clocks in different organs coordinate together? Individual clocks could communicate both within (black arrows) and between (red arrows) organs in order to coordinate plant timing.

https://doi.org/10.1371/journal.pbio.3000407.g001

days at near-cellular resolution (Materials and methods). This reporter line was chosen because of its strong expression level and its similar spatial expression to other clock components [5].

In order to observe the endogenous component of the rhythms, we first imaged seedlings under LL, having previously grown them under LD cycles (LD-to-LL; Fig 2A and Materials and methods). Under the LD-to-LL condition we observed phase differences of *GI*::*LUC* expression between organs (Fig 2B and 2C). The cotyledon and hypocotyl peaked before the root, but the tip of the root peaked before the middle region of the root (Fig 2C, S1 Fig, and S1 Video). Furthermore, we observed a decrease in coherence between regions over time, with a range between the earliest and latest peaking region of 4.92 ± 3.79 h (mean ± standard deviation) in the first and 18.36 ± 5.67 h in the final oscillation. This is due to the emergence of period differences between all regions (Fig 2D). The cotyledon maintained a mean period of 23.82 ± 0.60 h, whereas the hypocotyl and root ran at 25.41 ± 0.91 h and 28.04 ± 0.86 h, respectively. However, the root tip ran slightly faster than the middle of the root, with a mean period of 26.90 ± 0.45 h, demonstrating the presence of endogenous period differences across all regions. We verified that our results were not specific to the *GI*::*LUC* reporter, as we observed similar differences in periods and phases across the plant using luciferase reporters for promoter activity of the core clock genes *PSEUDO-RESPONSE REGULATOR 9* (*PRR9*) [31], *TIMING OF CAB EXPRESSION 1* (*TOC1*) [32], and *EARLY FLOWERING 4* (*ELF4*; S2 Fig) [33]. These observations are also qualitatively similar to the periods and phases previously observed in isolated organs [6,22,24], and at the cellular level across the seedling [5], validating our whole-plant assay for the circadian clock.

The phase at which a rhythm entrains to the environment can depend on the mismatch between its endogenous period and the period of the entraining signal [34–36]. We therefore tested the consequence of endogenous period differences between organs on the entrainment

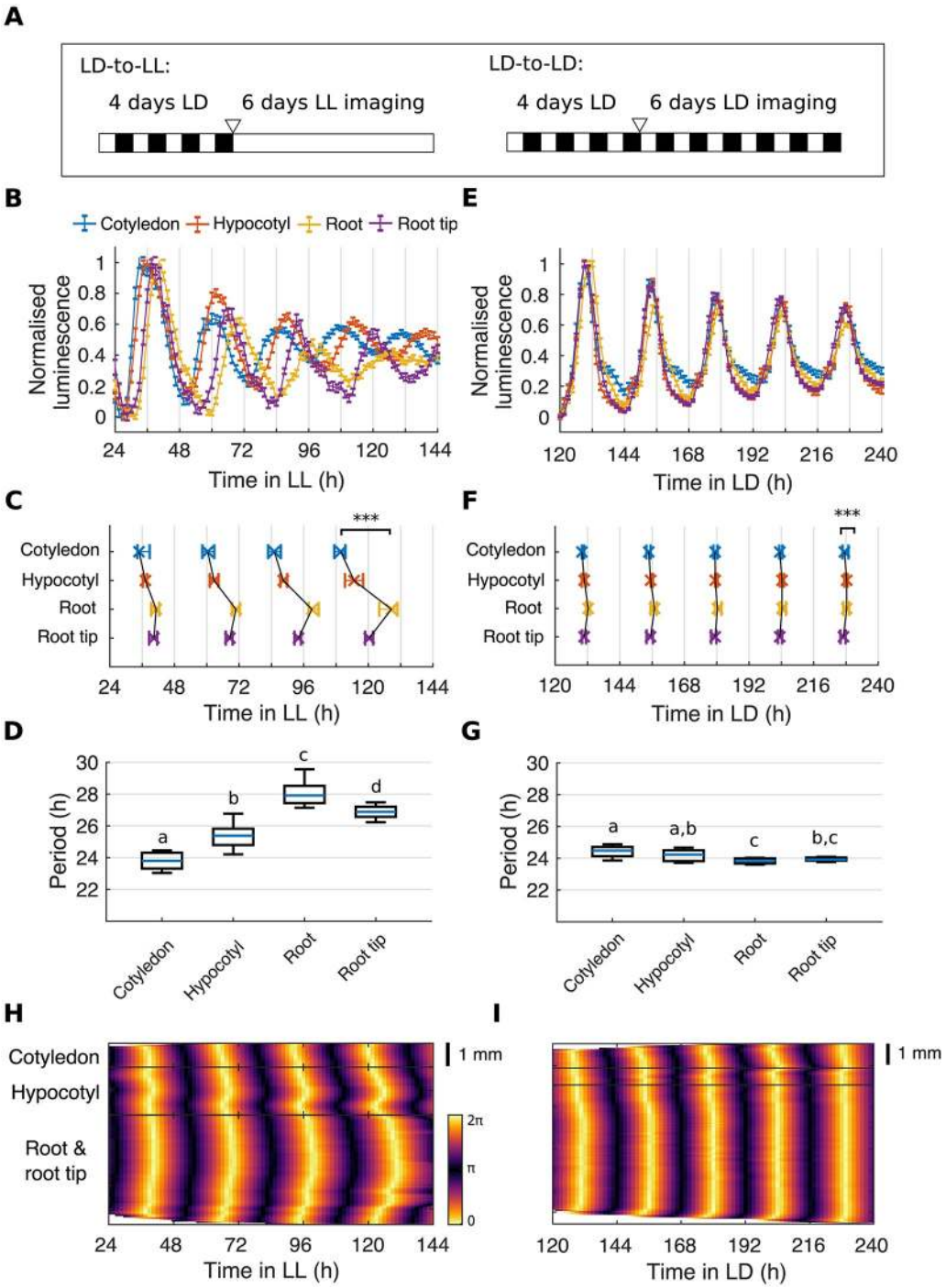

Fig 2. Organ-specific clocks show phase differences under constant environmental conditions and LD cycles. (A) Schematic depicting the experimental conditions used. Seedlings were grown for 4 d under LD cycles and imaged either under constant light (LD-to-LL) or LD (LD-to-LD). The white triangle represents the beginning of imaging. (B) Expression of *GI*::*LUC* from different organs imaged under the LD-to-LL condition. Data represent the mean ± standard error of organs scored as rhythmic. Luminescence counts were normalized to the minimum and maximum values of the time series. (C) Times of peaks of *GI*::*LUC* expression in different organs under the LD-to-LL condition. Plots represent the 25th percentile, median, and the 75th percentile for the peak times of organs scored as rhythmic. Organs show significant phase differences, $^{***}p < 0.001$, by Kruskal-Wallis ANOVA. Pairwise comparisons are shown in S1 Fig. (D) Period estimates of *GI*::*LUC* for different organs imaged under the LD-to-LL condition. The means of organs are statistically different ($p < 0.05$, by one-way ANOVA, Tukey post hoc tests) if they do not have a letter in common. (E) Expression of *GI*::*LUC* from different organs imaged under the LD-to-LD condition. Data represent the mean ± standard

error of organs scored as rhythmic. Luminescence counts were normalized to the minimum and maximum values of the time series. Color legend is as in B. (F) Times of peaks of *GI*::*LUC* expression in different organs imaged under the LD-to-LD condition. Plots represent the 25th percentile, median, and the 75th percentile for the peak times of organs scored as rhythmic. Organs show significant phase differences, $^{***}p < 0.001$, by Kruskal-Wallis ANOVA. Pairwise comparisons are shown in S3 Fig. Color legend is as in C. (G) Period estimates of *GI*::*LUC* for different organs imaged under the LD-to-LD condition. The means of organs are statistically different ($p < 0.05$, by one-way ANOVA, Tukey post hoc tests) if they do not have a letter in common. (H, I) Representative phase plot of *GI*::*LUC* expression across longitudinal sections of the cotyledon (top), hypocotyl (middle), and root (bottom) of a single seedling under LD-to-LL (H) and LD-to-LD (I) conditions. Color bars are as in H. For LD-to-LL data, $N = 4$; LD-to-LD, $N = 3$; for both, $n = 26–35$. *N* represents the number of independent experiments and *n* the total number of organs tracked. See S1 and S2 Files for exact *n*, test statistics, and percentage rhythmicity of each organ. Box plots indicate the median and upper and lower quartiles, and whiskers the 9th and 91st percentiles of organs scored as rhythmic. Underlying data are available from https://gitlab.com/slcu/teamJL/greenwood_etal_2019. *GI*, *GIGANTEA*; LD, light-dark; LL, constant light; *LUC*, *LUCIFERASE*.

https://doi.org/10.1371/journal.pbio.3000407.g002

of the plant, by monitoring *GI*::*LUC* rhythms under LD cycles (LD-to-LD; Fig 2A and Materials and methods). Under the LD-to-LD condition, we observed robust and entrained rhythms (Fig 2E). However, closer inspection of the timing of the peaks of the oscillations revealed significant differences in clock phase between organs (Fig 2F). The cotyledon and hypocotyl consistently peaked earlier than the root regions, but the root tip peaked earlier than the middle of the root (Fig 2F, S3 Fig and S2 Video). This is qualitatively similar to the pattern observed under LL (Fig 2C). However, under the LD-to-LD condition, the organs showed a more stable phase relationship than under LL, with a range between the earliest and latest peaking region of 2.08 ± 1.56 h in the first oscillation and 1.10 ± 1.44 h in the final oscillation. This is due to the fact that all organs oscillate with a period of approximately 24 h (Fig 2G).

Spatial waves of clock gene expression propagate between and within organs

Spatial waves of clock gene expression have been previously reported in plant leaves [18,19,25,26] and roots [5,20,27] under LL. However, their relation to one another and the relevance under LD cycles remained unclear. We analyzed our LD-to-LL and LD-to-LD data set of whole, intact seedlings at the sub-tissue level in order to address these questions. We extracted the phase of the luminescence signal across longitudinal sections of seedlings (S4 Fig, Materials and methods) and present phase plots and time-lapse videos of single seedlings representative for each light condition (Fig 2H and 2I, S1 and S2 Videos). The clearest waves of expression could be observed in the LD-to-LL condition, as phase differences increased with time. In the cotyledon, a wave of *GI*::*LUC* expression propagated from the tip to the base (Fig 2H, top), and downwards into the hypocotyl (Fig 2H, middle). In the hypocotyl, we observed a second wave traveling from the root junction upwards into the hypocotyl (Fig 2H, middle). Finally, within the root we observed two waves: one propagating down from the hypocotyl junction and the second from the root tip upwards into the root, as we have reported previously (Fig 2H, bottom) [5]. Evidence of waves of clock gene expression could also be observed under the LD-to-LD condition. Although they are less pronounced, small phase waves could be discerned within the cotyledon (Fig 2I, top), hypocotyl (Fig 2I, middle), and root (Fig 2I, bottom) of the phase plots and time-lapse videos (S2 Video).

Spatial waves of clock gene expression persist in the absence of interorgan communication

Previous work has proposed that spatial waves of clock gene expression are driven by local cell-cell coupling [5,18–20]. However, plant cells can communicate through both local and long-distance, interorgan pathways [29], and the root clock has been proposed to be driven by

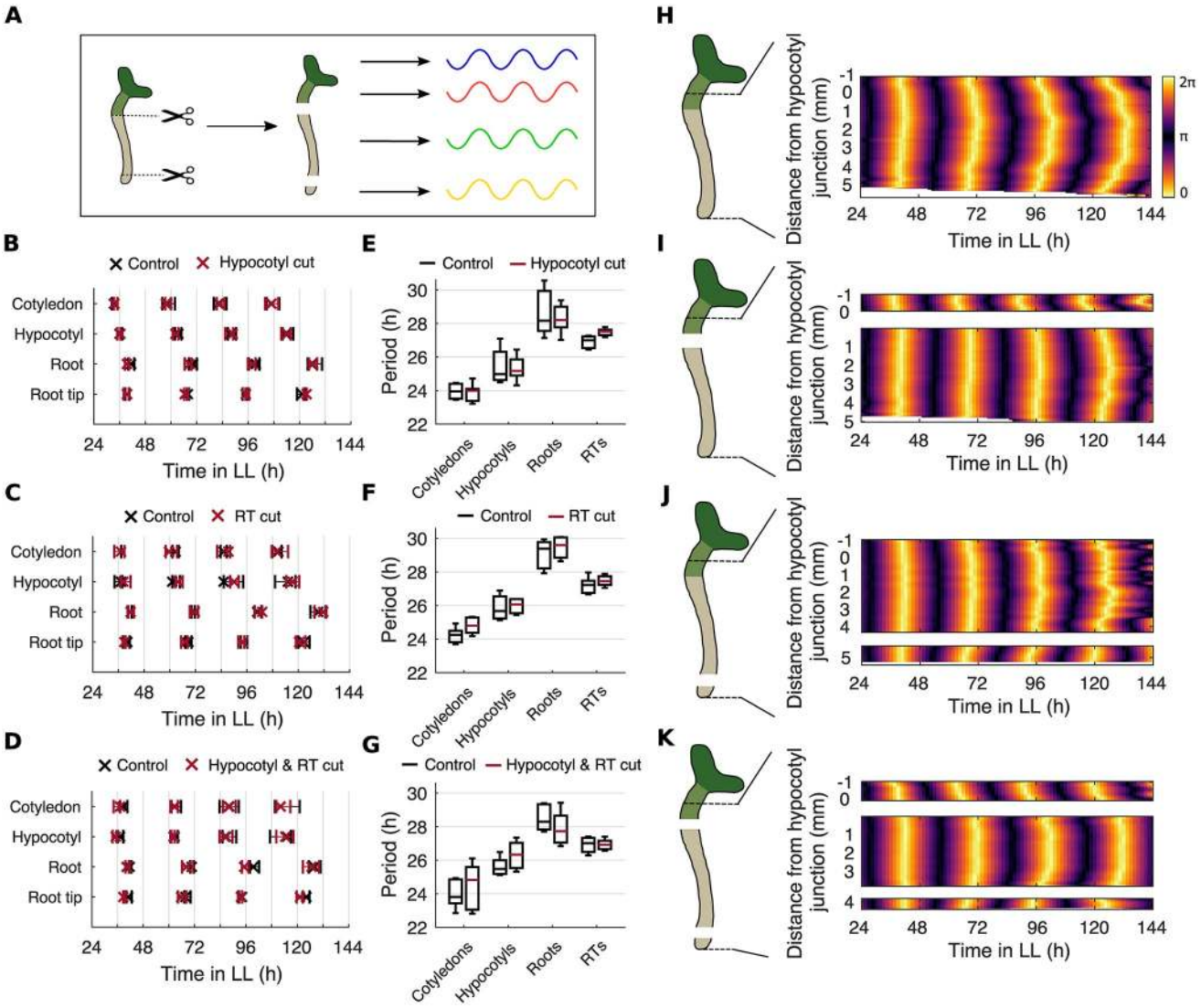

Fig 3. Spatial waves of clock gene expression persist in the absence of long-distance signals. (A) Schematic depicting the experimental design. Seedlings were cut at the hypocotyl junction, RT, or at both the hypocotyl junction and the RT. The rhythm of both the excised organs and the remaining intact organs were subsequently analyzed. (B–D) Times of peaks of *GI*::*LUC* expression in different organs following a cut at the hypocotyl junction (B), RT (C), or both the hypocotyl junction and RT (D). Plots represent the 25th percentile, median, and the 75th percentile for the peak times of organs scored as rhythmic. (E–G) Period estimates of *GI*::*LUC* for different organs following a cut at the hypocotyl junction (E), RT (F), and both the hypocotyl junction and RT (G). All comparisons of means are not significantly different, $p > 0.05$, by two-tailed *t* test, Welch correction. Box plots indicate the median and upper and lower quartiles, and whiskers the 9th and 91st percentiles of organs scored as rhythmic. (H–K) Representative phase plot of *GI*::*LUC* expression across longitudinal sections of the hypocotyl and root of a single seedling without a cut (H) or with a cut at either the hypocotyl junction (I), RT (J), or both the hypocotyl junction and RT (K). Schematics show the approximate cut position and the region analyzed. Color maps are as in H. For hypocotyl cut experiments, $N = 4$; RT cut, $N = 3$; hypocotyl and RT cut, $N = 3$. For all, $n = 9–17$. *N* represents the number of independent experiments and *n* the total number of organs tracked. See S1 and S2 Files for exact *n*, test statistics, and percentage rhythmicity of each organ. Underlying data are available from https://gitlab.com/slcu/teamJL/greenwood_etal_2019. *GI*, *GIGANTEA*; LL, constant light; *LUC*, *LUCIFERASE*; RT, root tip.

https://doi.org/10.1371/journal.pbio.3000407.g003

long-range signals from the shoot [9,22,24]. To investigate whether rhythms and spatial waves are driven by long-distance communication, we blocked signal transmission between organs by cutting the seedling into sections. We cut the root at either the hypocotyl junction, the root tip, or both the hypocotyl junction and the root tip, and then monitored the rhythms under LL (Fig 3A). We found that sectioning the plant did not substantially affect the phase of the

rhythms (Fig 3B–3D). Some minor phase differences were observed between cut and uncut controls after cutting, but these were no longer apparent after 6 d (S5 Fig). Period differences across the plant also persisted after cutting (Fig 3E–3G). Next, we focused our analysis to within the hypocotyl and root, where the simple geometry means the wave patterns can be most easily observed. Strikingly, after all cuts we observed the persistence of waves propagating both from the hypocotyl down into the root and from the root tip upwards (Fig 3I–3K and S3 Video). Our results show that in all organs excised, rhythms are autonomous, and the spatial waves that travel between them are not dependent on a long-distance signal.

Period differences plus local coupling can explain organ-specific entrainment and spatial waves

The persistence of rhythms and spatial waves in the absence of long-distance communication suggests clocks may instead be coupled through local interactions. We extended the mathematical framework we employed in previous work [5] to investigate whether local coupling can explain the entrainment behaviors that we observe under LD and LL. As before, we used a Kuramoto phase oscillator model [37]. In this framework, each pixel (which in fact represents multiple cells) on our seedling template is an individual oscillator with an intrinsic period and is weakly coupled to its nearest neighbors (S6 Fig). The intrinsic period of each pixel was set according to its location in the seedling. Pixels from the cotyledon, hypocotyl, root, and root tip were drawn from distributions centered around the mean periods that we observed experimentally in each region under LL (Fig 4A, S6 Fig, Materials and methods). These period estimates were made from in vivo experiments and therefore include the effects of coupling. They are, however, as good an estimation of the cell autonomous periods as possible in a physiologically relevant context. In our LD-to-LL simulations, because of the differences in intrinsic periods, and coupling, we saw increasing phase shifts between organs (Fig 4C) and two increasingly large waves in the root (Fig 4E), as observed in experiments (Fig 4G). We observed these spatial waves in simulations under a range of coupling strengths, K (S7 Fig). As the coupling strength was increased, the distribution of periods and phases of the oscillation became tighter, as previously reported in models of coupling in the SCN (S8 and S9 Figs) [38].

In our model, the amount that each oscillator phase is shifted is set by the mismatch of its intrinsic period and the period of the entraining rhythm [34–36]. This prediction is supported by experimental evidence in various organisms, including plants [39], although dawn can also reset the phase of some clock genes in bulk *Arabidopsis* experiments [40,41]. We tested whether the phase differences that we observe between organs in *Arabidopsis* under our LD conditions can be reproduced in our model by this mismatch with the entraining rhythm. In our simulations, organs were forced to oscillate with a period of approximately 24 h, due to entrainment to the external rhythm (Fig 4B). However, because of the mismatch between the intrinsic period and the entraining rhythm, organs entrained with different phases, matching those observed experimentally (Fig 4D). Phase shifts could also be observed at the sub-tissue level; two short waves could be observed in the root (Fig 4F), as in experiments (Fig 4H).

Local coupling limits desynchrony in the absence of entrainment

In a set of coupled oscillators, variation in period causes a decrease in synchrony, whereas coupling and external entrainment maintain or increase synchrony [42–45]. In order to make predictions about the presence of local coupling in seedlings, we simulated our model in the absence of LD entrainment. We simulated the duration of the experiment without entraining the oscillators, and thus assume that the phases are initially random (LL-to-LL; Fig 5A, Materials and methods). In contrast to the LD-to-LL condition, in which oscillators begin

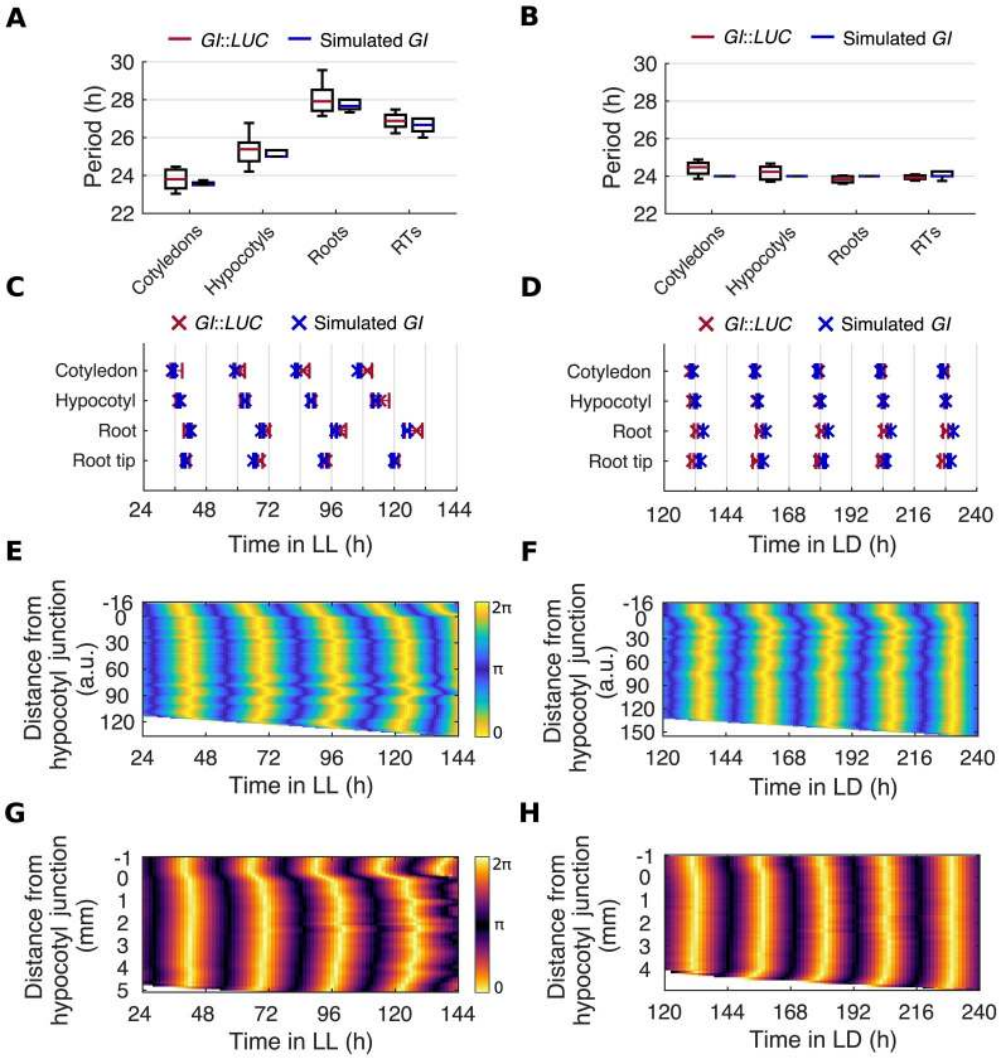

Fig 4. Period differences and local coupling can explain spatial waves of clock gene expression. (A, B) Period estimates of *GI*::*LUC* and simulated *GI* for different organs imaged under LD-to-LL (A) and LD-to-LD (B) conditions. Box plots indicate the median and upper and lower quartiles, and whiskers the 9th and 91st percentiles of organs scored as rhythmic. (C, D) Times of peaks of expression of *GI*::*LUC* and simulated *GI* in different organs under LD-to-LL (C) or LD-to-LD (D) conditions. Plots represent the 25th percentile, median, and the 75th percentile for the peak times of the oscillations of organs scored as rhythmic. (E, F) Representative phase plot of simulated *GI* expression across longitudinal sections of the hypocotyl and root of a single seedling under LD-to-LL (E) or LD-to-LD (F) conditions. Color maps are as in E. (G, H). Representative phase plot of *GI*::*LUC* expression across longitudinal sections of the hypocotyl and root of a single seedling under LD-to-LL (G) and LD-to-LD (H) conditions. Color maps are as in G. For experimental data, *N* and *n* are as in Fig 2. For *GI* simulations, $n = 24$. *N* represents the number of independent experiments and *n* the total number of organs tracked. See S1 and S2 Files for exact *n*, test statistics, and percentage rhythmicity of each organ. Underlying data are available from https://gitlab.com/slcu/teamJL/greenwood_etal_2019. *GI*, *GIGANTEA*; LD, light-dark; LL, constant light; *LUC*, *LUCIFERASE*; RT, root tip.

https://doi.org/10.1371/journal.pbio.3000407.g004

synchronous but become less synchronized whilst under LL, in LL-to-LL simulations, oscillators began less synchronous but maintained their order over the time course (Fig 5B). Interestingly, in the root, the model predicted a complex spatial pattern, with multiple phase clusters and spatial waves in a single seedling (Fig 5C and S4 Video). These patterns of gene expression were similar to the zigzag patterns previously reported by others, when roots are grown on

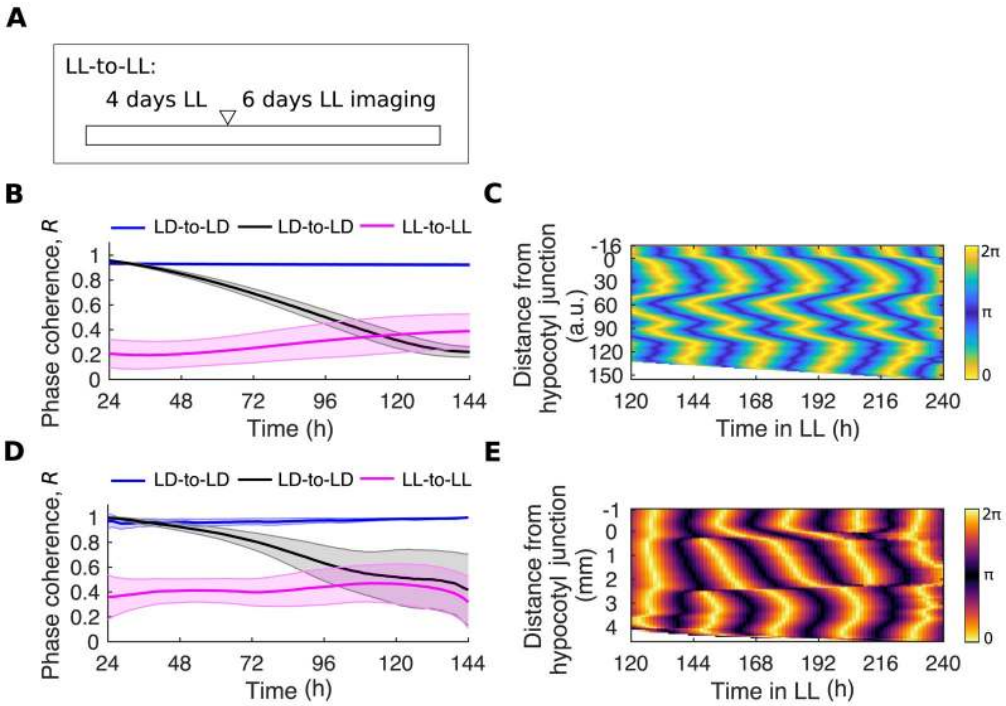

Fig 5. Local coupling limits desynchrony in the absence of LD cycles. (A) Schematic depicting the experimental conditions used. Seedlings were grown for 4 d under LL and then imaged, also under LL (LL-to-LL), so that seedlings have never seen an LD cycle. The white triangle represents the beginning of imaging. (B) Quantification of phase coherence by time evolution of the Kuramoto order parameter, *R*, for simulated *GI* expression. Solid lines indicate the mean and the shaded region one standard deviation of the mean. (C) Representative phase plot of simulated *GI* expression across longitudinal sections of the hypocotyl and root of a single seedling under the LL-to-LL condition. (D) Quantification of phase coherence by time evolution of the Kuramoto order parameter, *R*, for *GI*::*LUC* expression. Solid lines indicate the mean and the shaded region one standard deviation of the mean. (E) Representative phase plot of *GI*::*LUC* expression across longitudinal sections of the hypocotyl and root of a single seedling under the LL-to-LL condition. For LL-to-LL *GI*::*LUC* data, $N = 3$ and $n = 30$; for *GI* model simulations, $n = 24$. *N* represents the number of independent experiments and *n* the total number of organs tracked. See S2 File for exact *n*, test statistics, and percentage rhythmicity in each organ. Underlying data are available from https://gitlab.com/slcu/teamJL/greenwood_etal_2019. a.u., arbitrary unit; *GI*, *GIGANTEA*; LD, light-dark; LL, constant light; *LUC*, *LUCIFERASE*.

https://doi.org/10.1371/journal.pbio.3000407.g005

sucrose supplemented media [20,27,46]. We found that these zigzag patterns emerged with, but not without, local coupling (S10 Fig).

An alternative mechanism to explain the spatial patterns of rhythms that we observed can also be envisaged. If, within the tissue, there exists a gradient in the periods of oscillators, spatial waves may be seen in the absence of cellular coupling. Simulations of this plausible alternative model, without coupling but with a gradient of the intrinsic periods within the root, were indeed sufficient to generate simple waves similar to those we observed under the LD-to-LL condition (S10C and S10D Fig), but not the complex zigzag waves predicted in the LL-to-LL condition (S10E and S10F Fig).

In order to test our model and validate the assumption of local coupling, we experimentally tested the LL-to-LL model prediction. We both grew and imaged seedlings under LL conditions (LL-to-LL; Fig 5A), so that seedlings never see an entrainment cue beyond germination [47,48]. Roots maintain their coherence over the full time course (Fig 5D) and display a zigzag expression pattern (Fig 5E and S11 Fig) as predicted by the model, supporting the hypothesis of weak, local coupling.

Local light inputs set organ-specific periods

To test our model further, we attempted to manipulate the periods in specific organs to determine whether we could modulate the spatial waves of gene expression. In the most severe case, removing all period differences across the plant should result in perfectly coherent rhythms. We found mutations to the core clock network to have little effect on the organ specificity of periods in organs scored as rhythmic (S12 Fig). However, there were some organ-specific effects on rhythmicity (S1 File). We also note that we cannot rule out that mutations to other clock components could have a larger effect on the organ specificity of periods.

Next, we tested whether we could alter periods in an organ-specific manner by modulating inputs to the clock. We first tested the effect of light input by growing seedlings under LD cycles before imaging seedlings under constant darkness (DD). Under DD, we observed a drastic slowing of periods in the cotyledon and hypocotyl, whereas the middle region of the root maintained its speed compared with LL (Fig 6A). This is in contrast to previous lower-resolution work that found the period of the root as a whole increased under DD [28]. The lengthening of periods in the aerial organs reduced the phase differences between the aerial organs and the root (Fig 6B and S13 Fig), resulting in the loss of the spatial wave traveling from the hypocotyl down the root (Fig 6C and S5 Video). Inversely, in the root tip we observed a decrease in period compared with LL (Fig 6A), causing larger phase shifts between the root tip and the root (Fig 6B and S13 Fig) and resulting in a longer spatial wave traveling from the

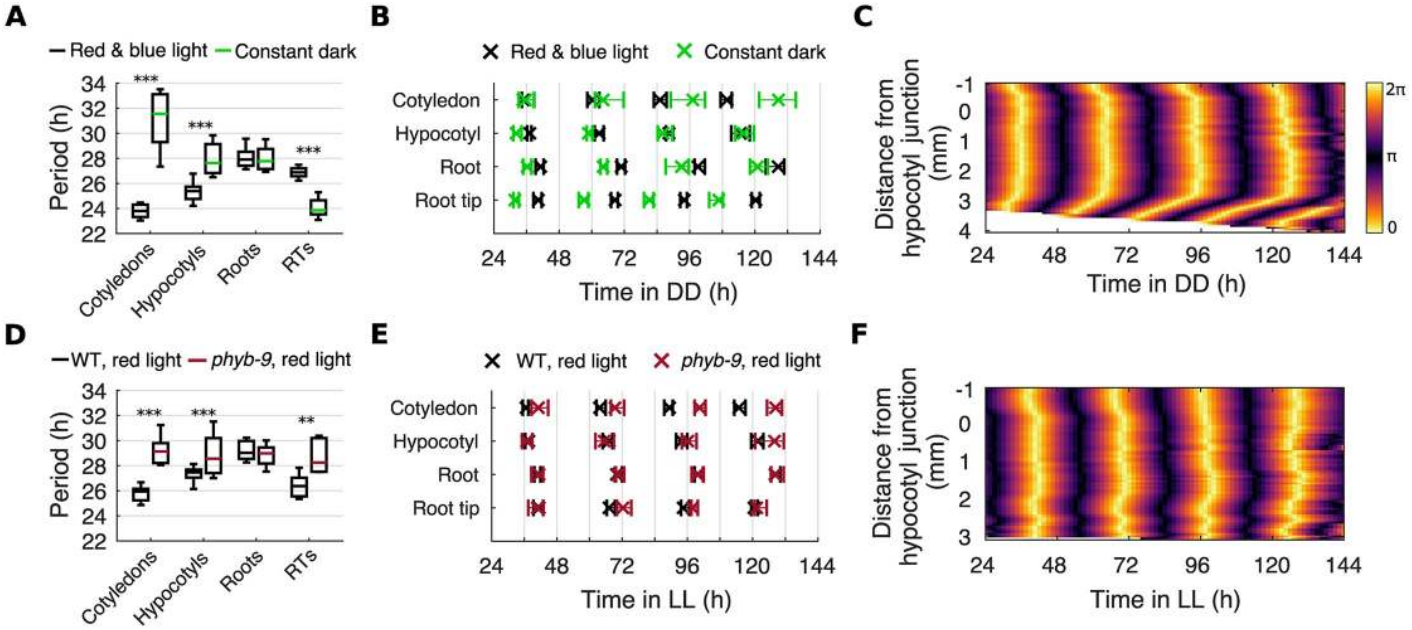

Fig 6. Local light inputs modulate the spatial coordination of the clock. (A) Period estimates for different organs under constant red and blue light or DD. $^{***}p < 0.001$, by two-tailed *t* test, Welch correction. (B) Times of peaks of *GI*::*LUC* expression in different organs under constant red and blue light or DD. Plots represent the 25th percentile, median, and the 75th percentile for the peak times of organs scored as rhythmic. (C) Representative phase plot of *GI*::*LUC* expression across longitudinal sections of the hypocotyl and root of a single seedling under DD. (D) Period estimates of *GI*::*LUC* for different organs under constant red light in the *phyb-9* mutant. $^{**}p < 0.01$, $^{***}p < 0.001$, by two-tailed *t* test, Welch correction. (E) Times of peaks of *GI*::*LUC* expression in different organs under constant red light in the *phyb-9* mutant. Plots represent the 25th percentile, median, and the 75th percentile for the peak times of organs scored as rhythmic. (F) Representative phase plot of *GI*::*LUC* expression across longitudinal sections of the hypocotyl and root of a single seedling under constant red light in the *phyb-9* mutant. For red and blue light data, *N* and *n* are as presented in Fig 2. For DD, $N = 3$; *phyb-9* red light, $N = 4$. For all, $n = 23–35$. *N* represents the number of independent experiments and *n* the total number of seedlings. See S1 and S2 Files for exact *n*, test statistics, and percentage rhythmicity in each organ. Box plots indicate the median and upper and lower quartiles, and whiskers the 9th and 91st percentiles of organs scored as rhythmic. Underlying data are available from https://gitlab.com/slcu/teamJL/greenwood_etal_2019. DD, constant darkness; *GI*, *GIGANTEA*; LL, constant light; *LUC*, *LUCIFERASE*; RT, root tip; WT, wild type.

https://doi.org/10.1371/journal.pbio.3000407.g006

root tip upwards into the root (Fig 6C and S5 Video). We observed the same effect when seedlings were grown so that the roots were not exposed to light during entrainment or imaging (S14 Fig). Additionally, a qualitatively similar but lesser effect was observed under monochromatic red or blue light (S15 Fig). Together, our experiments show that light input can set the periods of oscillators across the plant, either increasing or decreasing the speed, depending on the region. These differences are sufficient to drive spatial waves of gene expression between organs.

We next tested whether the effect of light on organ specificity is direct, through known light signaling pathways. We imaged *GI*::*LUC* expression in the *phyb-9* background, a null mutant for the primary red light photoreceptor in *A. thaliana*, *PHYTOCHROME B* (*PHYB*) [49,50]. Because *PHYB* has a tissue-specific expression pattern in the plant [51–54], we reasoned that its period-shortening effect under red light [55] may be organ specific. Under red light, in the *phyb-9* mutant we observed the loss of period differences between the cotyledon, hypocotyl, and root (Fig 6D). This caused the loss of phase shifts between the aerial organs and the root (Fig 6E and S16A Fig) and the loss of a distinct spatial wave traveling down the root (Fig 6F and S6 Video). We also observed a decrease in rhythmicity across the seedling (S1 File). The effect was particularly large in the root tip, with only 24% of root tips classed as rhythmic compared with 96% in the wild type. In the root tips classed as rhythmic, the period ran approximately 3 h slower, at approximately the same speed as the middle of the root (Fig 6D). Therefore, after 6 d under constant red light, the phase shifts between the root tip and root (Fig 6E and S16A Fig), and the spatial wave traveling from the root tip upwards, were attenuated (Fig 6F and S6 Video). The *phyb-9* mutation, however, does not abolish the faster periods observed in the root tip under DD (S16B and S16C Fig).

Local metabolic inputs set organ-specific periods

In addition to the external environment, the circadian clock is exposed to biochemical signals from within the cell [56]. We investigated whether these endogenous signals could also alter periods in an organ-specific manner, modulating the spatial waves of clock gene expression. First, we imaged seedlings under LL in the presence of 3-(3,4-dichlorophenyl)-1,1-dimethylurea (DCMU), a specific inhibitor of photosynthesis. During inhibition, we observed a slowing of periods specifically in the cotyledon and hypocotyl (Fig 7A), causing a loss of phase shifts between the hypocotyl and root (Fig 7B and S17 Fig) and the loss of the spatial wave down the root (Fig 7C).

Photosynthesis modulates the clock through the production of sugars, which feed into the oscillator [57–59]. We next tested whether the application of sucrose to part of the plant could locally reduce clock periods and generate spatial waves. This is a direct test of the hypothesis that local period differences drive spatial waves of gene expression. We designed a protocol that allowed us to rest only the top portion of the root on sugar-supplemented media and observe the effect throughout the root. We did this with roots cut at the hypocotyl junction to minimize developmental effects, and under DD, where we ordinarily observe no spatial waves down the root (Fig 7D). In comparison with mannitol (a poorly metabolized sugar that acts as an osmotic control), contact with sucrose-supplemented media caused a larger decrease in period length (Fig 7E). This caused larger phase shifts from the top to the middle of the root (Fig 7F and S18 Fig). Within the root, a clear spatial wave of clock gene expression propagates down from the top of the root when in contact with the sucrose (Fig 7G and S7 Video) but not mannitol (Fig 7H and S8 Video) supplemented media. Together these results show that altering the speed of clocks locally, either via modulating light perception or the addition of photosynthetic sugars, can drive spatial waves of clock gene expression.

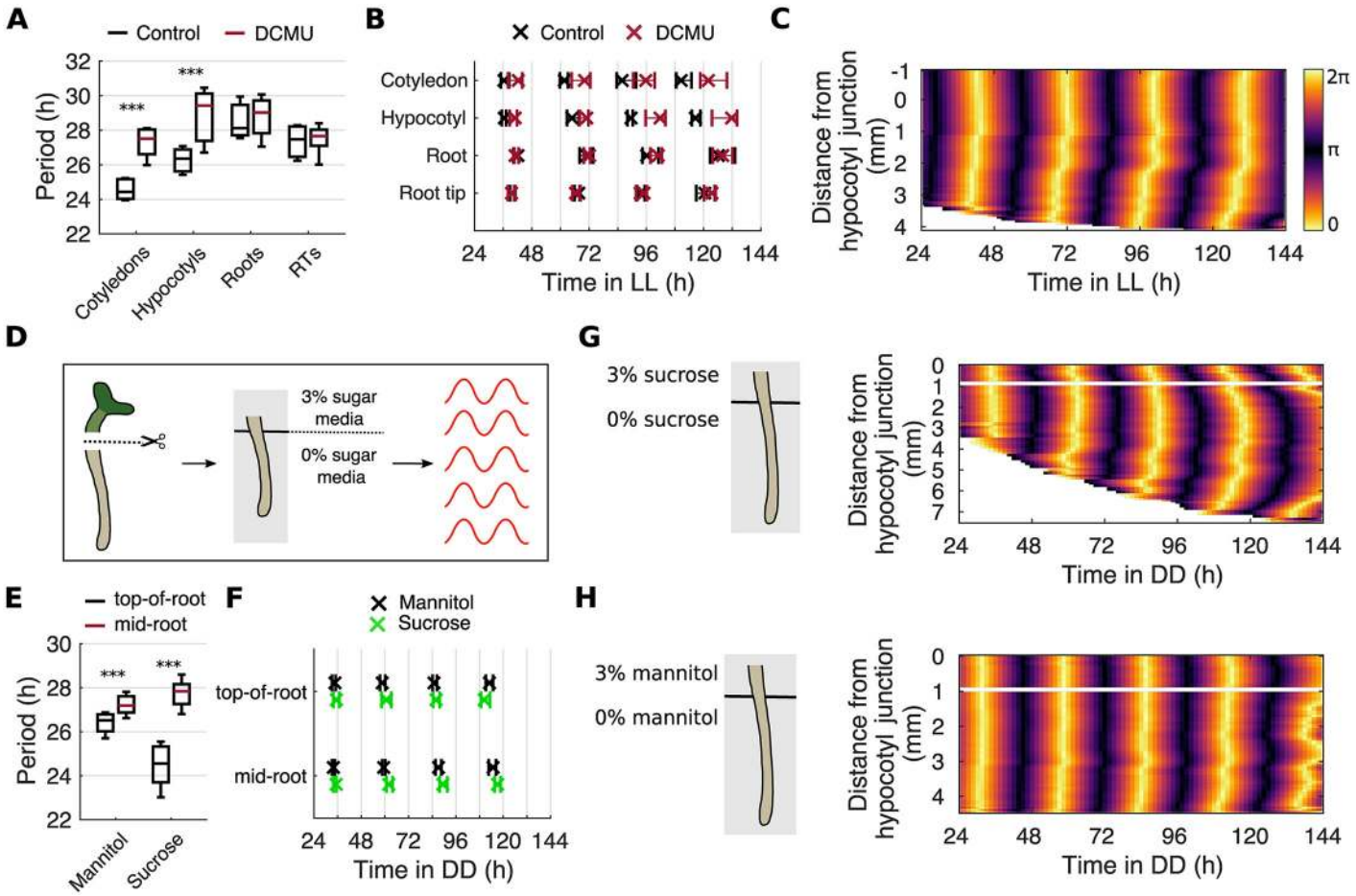

Fig 7. Photosynthetic sugar can drive spatial waves of clock gene expression by altering periods locally. (A) Period estimates of *GI*::*LUC* for different organs during the inhibition of photosynthesis by DCMU. $^{***}p < 0.001$, by two-tailed *t* test, Welch correction. (B) Times of peaks of of *GI*::*LUC* expression in different organs during the inhibition of photosynthesis by DCMU. Color legend is as in A. Plots represent the 25th percentile, median, and the 75th percentile for the peak times of organs scored as rhythmic. (C) Representative phase plot of *GI*::*LUC* expression across longitudinal sections of the hypocotyl and root of a single seedling during the inhibition of photosynthesis by DCMU. (D) Schematic representing the experimental design. Seedlings are cut at the hypocotyl junction and the excised root laid across two adjacent agar pads, one containing sugar-supplemented media and the other not, so that only the top part of the root is in contact with sugar. Roots are then imaged under DD. (E) Period estimates of *GI*::*LUC* for the top and middle regions of the root during the partial contact of the root with sucrose or mannitol, under DD. $^{***}p < 0.001$, by two-tailed *t* test, Welch correction. (F) Times of peaks of *GI*::*LUC* expression for the top and middle regions of the root during the partial contact of the root with exogenous sucrose or mannitol, under DD. Plots represent the 25th percentile, median, and the 75th percentile for the peak times of organs scored as rhythmic. (G, H) Representative phase plot of *GI*::*LUC* expression across longitudinal sections of the hypocotyl and root of a single seedling during the partial contact of the root with exogenous sucrose (G) or mannitol (H), under DD. Schematic shows the approximate position of the root on the agar pads. Color bars are as in C. For DCMU, $N = 3$; exogenous sucrose, $N = 3$; exogenous mannitol, $N = 2$. For all, $n = 8–30$. *N* represents the number of independent experiments and *n* the total number of organs tracked. See S1 and S2 Files for exact *n*, test statistics, and percentage rhythmicity in each organ. Box plots indicate the median and upper and lower quartiles, and whiskers the 9th and 91st percentiles of organs scored as rhythmic. Underlying data are available from https://gitlab.com/slcu/teamJL/greenwood_etal_2019. DCMU, 3-(3,4-dichlorophenyl)-1,1-dimethylurea; DD, constant darkness; *GI*, *GIGANTEA*; LL, constant light; *LUC*, *LUCIFERASE*; RT, root tip.

https://doi.org/10.1371/journal.pbio.3000407.g007

Discussion

Here, we report how local periods, because of differences in sensitivity to clock inputs, can generate spatial waves of circadian clock gene expression across the plant. Using time-lapse imaging we show that spatial waves exist both in constant and entrained conditions and do not require long-distance signals. Modeling and experiments show that local coupling can explain our results, including complex synchronization patterns in plants that have never

seen an entraining signal. Finally, by the manipulation of environmental inputs, we are able to modulate the waves in a predictable manner by locally altering clock periods. We therefore propose that spatial waves are sufficient to integrate organ-specific environmental inputs and coordinate timing across the plant.

In the laboratory, clocks are most often studied under constant environmental conditions in order to observe the endogenous genetic properties of the oscillator. However, in the wild, plants are exposed to environmental cycles, and the interaction between the oscillator and the environment is of importance. It is therefore significant that we observed phase differences between clocks within a plant, even under LD cycles. A previous high-resolution study in *A. thaliana* observed phase differences within leaves after the transfer from LL to LD conditions, although rhythms were near synchronous after 3 d in LD cycles [18]. Phase differences have also been observed in *Lemna gibba* fronds, where cells in leaves entrain with different phases, causing a centrifugal pattern [21]. Phase patterns under LD cycles may therefore be a common property of plant circadian systems, and will require further investigation.

The presence of local cell-cell coupling has been previously suggested to help maintain clock synchrony within *A. thaliana* [5,18–22]. In addition, long-distance signals [22,24] and light piped from the shoot [28] have been proposed as mechanisms for coordination. Through a combination of experiments and modeling, we show that in seedlings, local signals alone are sufficient to maintain robust rhythms after 6 d in all organs, as well as generate the observed complex spatial patterns in clock expression. We note that our results do not exclude the possibility that phloem mobile signals, or light piped from the stem, additionally act to synchronize the root with the shoot. However, the waves that we observe in cut roots, combined with the wave up the root apparent in seedlings grown in DD, suggest that these signals do not drive the spatial wave patterns that we observe. In future work, it will be important to investigate whether coordination through local coupling also occurs in later stages of plant development and, if so, whether the coordination structure changes as the plant develops to compensate for its increasing size.

Local coupling is dependent on a signal that is cell-to-cell mobile. Research in cellular communication in plants has intensified in recent years and a number of signals are known to be mobile between cells and tissues. A selection of hormones, sugars, mRNAs, proteins, and ions have been shown to be both mobile and capable of influencing the clock [3,56]. To better understand the mechanism of intercellular coupling of clocks in plants, it will be important to investigate whether one, some, or all of these mobile signals act to couple the clock. Of particular interest is the transcription factor *ELONGATED HYPOCOTYL 5* [60], which moves locally and long distance [61], is activated by stem-piped light [62], and can influence the circadian clock [63–65]. As many components can move between cells, with, for example, thousands of mobile mRNA elements [66], single cell "omics" methods [67,68] will become increasingly important tools.

Oscillators in different organs of the plant are exposed to different conditions, both externally from the environment and internally from the cell's biochemistry. We found that these differences in input can drive spatial waves by creating period differences. We demonstrated this by manipulating two environmental inputs, light and sucrose, an external and internal signal, respectively. There are, however, many other signals known to modulate the speed of the clock [56]. In future work, it will be important to test how these interact and the consequence to spatial coordination when plants are under physiological conditions. Of particular interest will be temperature, which is known to differ between the air and the ground [69] and deviate from the photoperiod [70]. In fact, it has already been demonstrated that temperature is preferentially sensed by the clock in specific cell types [11,71]. Comprehensive in

vivo studies under a range of environmental conditions will be required to understand the full complexity.

Although it appears that clock coordination in plants is not centralized as it is in mammals, there remain interesting parallels between the two systems. Experimental and modeling studies have revealed that coupling between neurons generate spatial-temporal patterns of rhythmicity in the SCN itself, including wavelike patterns that depend on intercellular communication [38,72–74]. Although mammalian clocks have the additional complexity of the SCN driving rhythms in peripheral tissues across the rest of the organism, the similarities between the wave patterns observed in the SCN and in plant clocks are intriguing and could point to general principles of clock coordination. It will be important to examine the similarities and differences between the two systems in more detail in the future.

For plants, being responsive to the environment whilst being robust to fluctuations necessitates a trade-off. These fluctuations could be external, such as an environmental change, or internal, such as gene expression noise [75,76]. The clock, in its role as master regulator, must balance the competing requirements of flexibility and robustness. Recently, it has been proposed that the clock in plants is dynamically plastic, able to respond to changes in environmental inputs by altering its period and phase [77,78]. Cell-cell coupling increases the synchrony and robustness of oscillations, influencing how easy it is for clocks to entrain to the environment [79]. A decentralized structure with organ-specific inputs to clocks that are coupled together could allow some flexibility in sensing the environment whilst ensuring robust timing. In the future, it will be important to better understand the importance of this design principle in terms of the physiological outputs of the clock and the development of the plant.

Materials and methods

Plant materials and growth conditions

The wild-type *GI*::*LUC*, *PRR9*::*LUC*, and *TOC1*::*LUC* lines are in the Col-0 background and as described previously [80,81]. To produce the wild-type *ELF4*::*LUC* line, the promoter region of *ELF4* was amplified from *A. thaliana* genomic DNA using the primer pairs ELF4_prom_Fwd/Rev (ELF4_prom_Fwd, 5′- AGAGAATTCCTAAATCATCAAAGCCAACC-3′ and ELF4_prom_Rev, 5′-CTTTCTAGAAATAATTTTTAATTGTGTTTTTCTCTC-3′). Unique restriction sites were designed at the ends of the amplicons to facilitate cloning in the pPCV-LUC+ binary vector [82] via *EcoRI* (5′) and *XbaI* (3′) sites. The cloned *ELF4* promoter fragment was of 1,546 base pairs and contained the full 5′-untranslated region, but not the ATG. The construct was transformed into the Col-0 background by means of agrobacterium-mediated transfection [83]. Homozygous third generation lines were used for experiments.

The *phyb-9 GI*::*LUC* line is in the Col-0 background and as described previously [80]. The *cca1-11* (TAIR:1008081946; Ws background back-crossed with Col-0 three times) [84], *prr9-1* (TAIR:3481623) [85], *prr7-3* (TAIR:3662906) [85], *toc1-101* (TAIR:6533848449) [86], and *lux-4* (TAIR:1008810333) [87] alleles are loss-of-function mutations that have been previously described, and were transformed with the *GI*::*LUC* [80] construct by means of *Agrobacterium*-mediated transfection [83]. Homozygous third generation lines were used for experiments.

Seeds were surface sterilized and placed in the dark at 4 ˚C for 3 d. Seeds were sown at dawn of the fourth day on full-strength Murashige and Skoog (MS), 2% agar, pH 5.7 media, without sucrose unless otherwise specified. Seeds were then grown inside of plant growth incubators (MLR-352; Panasonic, Japan) for 4 d under 80 μmol m^2 s^{-1} cool white light at a constant temperature of 22 ˚C. Seedlings were grown under 12-h light–12-h dark cycles unless otherwise specified. Plates were orientated vertically during growth.

For experiments in which roots are grown in the dark (S14 Fig), seedlings were grown in full-strength MS liquid solution as described previously [88]. After 4 d of growth, working under green light only, seedlings were transferred to MS 2% agar plates and transferred to imaging cabinets.

Luciferase imaging

At dusk of the fourth day of growth, seedlings were sprayed with a 5 mM D-Luciferin (Promega, Madison, WI), 0.01% Triton X-100 solution (Sigma-Aldrich, St. Louis, MO). At dawn of the fifth day, 6–8 seedlings were transferred into a 3- by 3-cm area of the media plate in order to fit inside of the camera's field of view. Plates were orientated vertically during imaging.

Imaging was performed inside of growth incubators (MIR-154; Panasonic, Japan) at a constant temperature of 22 ˚C and under an equal mix of red and blue light–emitting diodes (40 μmol m^{-2} s^{-1} total), unless specified as red light only (40 μmol m^{-2} s^{-1} red) or blue light only (40 μmol m^{-2} s^{-1} blue). For experiments under LD cycles, lights were switched on to full intensity at dawn and completely off at dusk. Images were taken every 90 min for 6 d, with an exposure time of 20 min. Images were taken using a LUMO charge-coupled device camera (QImaging, Canada) controlled using Micro-Manager (V2.0; Open Imaging) as previously described [89,90]. The camera lens (Xenon 25 mm f/0.95; Schneider, Germany) was modified with a 5-mm optical spacer (Cosmicar, Japan) to increase the focal length and decrease the working distance.

Cuts and treatments

For cut experiments, seedlings were cut approximately 3 h after dawn of the fifth day of growth, immediately prior to the commencement of imaging. For "hypocotyl cut" experiments (Fig 3B, 3E and 3I), seedlings were cut in the root as close to the hypocotyl junction as discernible by eye; for "root tip cut" experiments (Fig 3C, 3F and 3J), seedlings were cut approximately 100–200 μm from the root cap. Cuts were made with a pair of Vanna's type microdissection scissors (Agar Scientific, UK). Following all excisions, the organs were gently separated with a pair of forceps to ensure no physical contact.

DCMU (Sigma-Aldrich, St. Louis, MO) was added to the media at a final concentration of 20 mM. Seedlings were transferred to the DCMU-containing media at dusk of the fourth day of growth. For sugar application experiments (Fig 7E–7H), media was added in 8-well rectangular dishes (NUNC; Thermo-Fisher Scientific, Waltham, MA) so that one well contains media supplemented with MS and sugar whilst the adjoining well contains media supplemented with MS only. Wells were filled with equal volumes to the brim of the wells so that the two agar pads form a continual flat surface but do not touch. Sucrose or mannitol (Sigma-Aldrich, St. Louis, MO) was added at a final concentration of 90 mM (3% w/v). Seedlings were cut at the hypocotyl junction (as described above) and laid across the adjoining agar pads so that approximately the top 1 mm of the excised root rests on the sugar-supplemented media, and the remainder of the root rests on the non-sugar-supplemented media. Seedlings were cut and transferred to the media at dawn of the fifth day of growth, immediately prior to the commencement of imaging.

Organ-level analysis of period and phase

For the organ-level analysis of the period and phase, organs were first tracked manually in Imaris (BitPlane, Switzerland) using the "Spots" functionality. We use a circular region of interest (ROI) of approximately 315-mm diameter and track the center of a single cotyledon, hypocotyl, root, and the root tip from each seedling. As the root grows, we maintain the root

ROI a fixed distance from the hypocotyl junction. A small number of cotyledons and hypocotyls were not trackable due to their orientation or their overlap with each other. These organs were excluded from the analysis. The median of the ROI was extracted to give the time series. Prior to the analysis of period and phase, the time series were first background subtracted. Very low expression rhythms with a minimum intensity value of less than zero after background subtraction were then removed. All time series were inspected by eye after preprocessing steps and prior to analysis.

Period analysis was conducted in BioDare2, a data server for the analysis of circadian data (biodare2.ed.ac.uk) [91]. All period estimates were performed on non-normalized data between 24–144 h from dawn of the day imaging began using the fast Fourier transform non-linear least squares (FFT-NLLS) algorithm [92,93]. Data were first baseline detrended by subtraction of a polynomial of degree three from the data. Oscillations were classed as rhythmic if the FFT-NLLS algorithm returned a period in the range of 18–36 h with a confidence level (as defined in [91]) below 0.6.

For the analysis of the times of peaks of expression, peaks were identified using the MATLAB (MathWorks, UK) "findpeaks" function. This was done after the application of a third-order Butterworth filter to remove high-frequency noise. Only peaks in which all organs complete the full cycle within 24–144 h from dawn of the day imaging are used. Additionally, peaks were discarded if they are closer than 18 h or further than 36 h apart.

Statistical analyses

In all figures, data points, measure of error, statistical test used, *N*, and the range of *n* are reported in the figure legend. Exact *p*-values, exact *n*, percentage rhythmicity, and other test statistics are reported in S1 and S2 Files. When values are described in the text, they are quoted as mean ± standard deviation of the mean. For the comparisons of period estimates, one-way ANOVA (with Tukey post hoc method) was used for comparisons of more than two groups, and the *t* test (with Welch correction) for comparison of two groups. For comparison of times of peaks of expression, the distribution is often skewed, therefore the Kruskal-Wallis one-way ANOVA (with Dunn post hoc method) was used for multiple comparisons and the Wilcoxon rank-sum test for comparison of two groups. An alpha level of 0.05 was used for all ANOVA tests.

Luciferase phase plots

To analyze spatial patterns within the organ, we first created space-time intensity plots of the luciferase images before obtaining a phase representation of the plots using a wavelet transform (henceforth called "phase plots"). These phase plots allowed interpretation of the space-time dynamics of the signal across the length of the organ independent of amplitude fluctuations.

Space-time intensity plots of the luciferase data were created as described previously [5], although with some modifications—most importantly of which, we include a modification that allowed us to better section curved roots. The method including modifications is outlined here in its entirety. Unless otherwise specified, steps are implemented via custom-developed MATLAB scripts.

Image preprocessing. A number of image processing steps were applied prior to the extraction of oscillations:

1. Each seedling was cropped into individual image stacks using ImageJ (NIH) in order to facilitate the further analysis.

2. A rectangle ROI encompassing the whole of the organ of interest plus the surrounding background was defined. When multiple organs were plotted together (Fig 2H and 2I), the regions are defined so that there are neither longitudinal gaps nor overlap between them. The ROI was manually checked for signal from neighboring organs or seedlings. These pixels were removed using ImageJ.
3. A 3-by-3 median filter was applied to the images to deal with background intensity spikes supposedly from cosmic rays and camera sensor imperfections.
4. The luminescent signal from the organ was segmented from background pixels by applying a threshold to each image individually. The mean of the intensity count across the whole ROI was used as the threshold value.
5. Small objects remaining in the image that are not connected to the organ were removed by applying a morphological opening algorithm. Connected objects less than 50 pixels are removed.

Intensity space-time plots. To create the space-time plot, we averaged the signal across longitudinal sections of the organ. However, because plant organs naturally curve during growth, we took our longitudinal sections to be perpendicular to the angle of growth. We did this as follows:

1. For an ROI of dimensions m,n (with m representing the horizontal dimension and n the vertical dimension), the grey-level-weighted centroid C across each vertical section n was calculated as

$$C^n(t) = \frac{\sum_{m=1}^{Np} m \cdot W_{m,n}(t)}{\sum_{m=1}^{Np} W_{m,n}(t)},$$

   where W represents the pixel intensity value and Np the width of the plant, as the number of segmented pixels.
2. A polynomial function of seventh degree was fitted to the centroids to give a curve that describes the shape of the hypocotyl and root $\{C(t)\}$ (S4A Fig).
3. At each horizontal position of the ROI $\{C^n(t): n = 1, 2, \ldots)\}$, the tangent and normal line was calculated (S4A Fig).
4. The slope of the normal line was rasterized to give pixel coordinates describing the line (S4B Fig). The Bresenham algorithm was utilized for this purpose [94], implemented in MATLAB [95].
5. The rasterized line was limited to 10 pixels, centered around the intersect with the curve fit $\{C(t)\}$. This prevents multiple intersects with the organ.
6. The mean intensity of the pixels corresponding to the coordinates was taken to give the intensity value for section n at time t in the space-time intensity plots (S4C Fig).

Phase space-time plots. We used the wavelet transform to obtain phase plots (S4D Fig) from intensity space-time plots (S4C Fig). The continuous wavelet transform is closely related to the Fourier transform. However, unlike the Fourier transform, the continuous wavelet transform does not assume a stationary signal [96,97]. This could be relevant to our data, given

that an oscillator response to perturbations may be transient or changing. This method has been used previously to analyze dynamic oscillations [98,99].

Given a time series $V = (V_1, \ldots, V_n)$, the continuous wavelet transform of V is given by

$$W_s(t) = \frac{1}{\sqrt{s}} \sum_{p=1}^{n} V_p Z^* \left(\frac{p-t}{s} \right),$$

where t represents time, Z is a wavelike function known as the mother wavelet, and s is a dimensionless frequency scale variable. Z^* denotes the complex conjugate of Z. For Z, we chose the Morlet wavelet,

$$Z(u) = \frac{e^{6iu} e^{-u^2/2}}{\pi^{1/4}},$$

an oscillatory function that depends on a dimensionless time, like parameter u, and is localized in time with zero mean [97]. The wavelet transform can instead be expressed in terms of its phase φ and magnitude q,

$$W_s(t) = q_s(t) e^{i\varphi_s(t)}.$$

For meaningful interpretation of the phase values, s must be chosen close to the characteristic period of the times series V. However, the resultant phases are robust to small variations of s. We therefore selected a single s for each organ, matching s to the frequency of the rhythms that we observed in the organ under the experimental condition. Carrying out this procedure for every row of the intensity kymographs resulted in a phase plot (S4D Fig) corresponding to the intensity plot (S4C Fig). For comparison between plots, we plotted the first 16 pixels (approximately 1 mm) of the hypocotyl and the entirety of the root.

Synchrony analysis

By looking at the all-to-all synchrony between pixels within the hypocotyl and root, the synchrony of oscillators in these tissues can be estimated. We excluded the cotyledons from the analysis because their orientation and movement make phase extraction difficult. For each time point, the order parameter [43] R at time t was obtained as

$$R(t) = \frac{1}{N} \sum_{j=1}^{N} e^{i\theta_j(t)},$$

where N is the total number of pixels in the hypocotyl and root combined and θ_j the phase of the j-th pixel. R values range from 0 to 1, with a value of 1 indicating a set of completely synchronized oscillators and a value of 0 a set of completely desynchronized oscillators.

Phase oscillator model

As in [5], we used the Kuramoto phase oscillator model to describe the dynamics of *GI::LUC* in each pixel (here, a pixel represents a set of individual, neighbor cells). We viewed the plant in two dimensions with positions in horizontal and vertical (longitudinal) directions described by index positions i and j, respectively, so that every pixel, $P(i,j)$, has an associated position, (i,j). The phase at the pixel $P(i,j)$ was represented by $\theta^{(i,j)}$, where its dynamics in time, t, are

governed by the following equation

$$\frac{d\theta^{(i,j)}}{dt} = \omega^{(i,j)} + K\sum_{\langle m,n\rangle} sin(\theta^{(m,n)} - \theta^{(i,j)}) - K_{LD}sin\left(\frac{\pi}{12}t - \theta^{(i,j)}\right).$$

Here, the first term is the intrinsic frequency of the pixel, $\omega^{(i,j)}$. The second term is the coupling contribution from the nearest-neighbor pixels in positions (m,n) that are closest to (i,j), namely $m = i-1, i, i+1$, while $n = i-1, i, i-1$. We assumed a plant template that is symmetric and resembles the shape of a seedling (S6 Fig). For the sake of simplicity, we assumed that the coupling constant, K, is the same across all pixels, and set it arbitrarily to $K = 1$ unless otherwise specified. The final term represents the coupling of the oscillator to the external force—in this case, the light force. Here, K_{LD} is the constant for the intensity of the light forcing, in which all oscillators are subject to 24-h forcing. Note that when the clocks are not entrained to the LD cycles, $K_{LD} = 0$. Because *GI* tends to peak at the onset of dusk in 12-h light–12-h dark cycles and shorter photoperiods [100], we assume that the phase of *GI* will be antiphase to light, hence the negative sign in front of K_{LD}. In our simulations of the LD-to-LD model, we set $K_{LD} = 1$.

Intrinsic periods are different across different sections of the plant. Intrinsic periods of the pixels in each section were taken from normal distributions with means of 23.82 h, 25.41 h, 29.04 h, and 26.90 h for cotyledon, hypocotyl, root, and root tip pixels, respectively, with the standard deviation at 10% of the mean value. The root tip is 5 pixels long and wide.

Initial values of all phases in the LD-to-LL and LD-to-LD simulations were at the time of the start of measurement identical, with first peaks occurring approximately 11 h after the first measurement. In the LL-to-LL model, because we had no information about the initial phases, we set them to be uniformly distributed across a cycle (i.e., random). We note that in the LL-to-LL model, setting the phases to be in phase or close to in phase (e.g., approximately 11 h after the first measurement ±2 h [standard deviation]), we could not obtain the results seen. ODEs were solved using the Euler method and simulations performed in MATLAB.

Because the seedlings in our experiments grow, we introduced growth to the template seedling: we allowed the root to grow by one pixel every 5 h. Every newborn cell (and hence the new pixel) had the same phase as the closest set of cells (pixels) in the template, namely new pixels $P(i, j)$, $P(i+1, j)$, and $P(i+2, j)$ will inherit the phases from $P(i, j-1)$, $P(i+1, j-1)$, and $P(i+2, j-1)$, respectively. Their periods were taken from the normal distribution, with the mean of 26.90 h and the standard deviation 10% of the mean value.

After root growth, the root tip should stay fixed in size (of 5-by-5 pixels), so the previous most upper set of root tip pixels at the root/root tip junction were, from then on, considered as root tissue instead. This means that their periods lengthen and they were chosen from a normal distribution with the mean of 28.04 h and the standard deviation 10% of the mean value.

The expression of *GI* for each pixel, $GI^{(i,j)}$, was calculated from the phase model as $GI^{(i,j)}(t) = \cos(\theta^{(i,j)}(t)) + 1$. It follows that the total sum of the luminescence for every longitudinal position j is $GItot^{(j)} = \sum_{i=1}^{n_j} GI^{(i,j)}$, where the total number of cells measuring across that section of the plant is n_j. The total luminescence was normalized so the maximum peak of expression in every longitudinal position is 1. The phases were extracted from the luminescence using the wavelet transform, as described above for the experimental data in 'Phase space-time plots'.

To calculate the periods of the tissues as shown in Fig 4A and 4B, we took regions of 5-by-5 pixels in each tissue (S6 Fig) and calculated the median *GI* expression level for each region. Periods were calculated as the mean of the peak-to-peak periods of the median trace. To observe the distributions of periods and phases within a single simulation of a seedling

(S8 and S9 Figs), we analyzed *GI* expression for all pixels on the plant template individually. Periods were calculated as the mean of the peak-to-peak periods, and phases were taken at $t = 96$ h. Due to growth of the seedling template, there were a small number of pixels with a short time series containing less than two peaks of expression. These pixels were excluded from the analysis.

An alternative model that could give rise to the LD-to-LL spatial wave behaviors observed is one where there is no coupling but periods increase towards the middle of the root. This means that $K = 0$, and we set periods in the root to increase linearly from 25.41 h at the hypocotyl/root junction to 28.04 h in the middle of the root, and then decrease linearly again to 26.90 h at the root/root tip junction. All other previous assumptions were adopted. Here, although a bow-shaped wave of expression could be obtained in the LD-to-LL simulations (S10C and S10D Fig), the model failed to reproduce the behavior observed in the LL-to-LL condition (S10E and S10F Fig).

Supporting information

S1 Fig. Organs show phase differences under constant environmental conditions from the first to the final oscillation. Times of peaks of *GI*::*LUC* expression in different organs during the first (left) and final (right) observed oscillations under the LD-to-LL condition. Means are statistically different ($p < 0.05$, one-way ANOVA, Tukey post hoc tests) if they do not have a letter in common. Box plots indicate the median and upper and lower quartiles, and whiskers the 9th and 91st percentiles of organs scored as rhythmic. *N* and *n* are as presented in Fig 2. See S2 File for exact *n*, test statistics, and percentage rhythmicity of each organ. Underlying data are available from https://gitlab.com/slcu/teamJL/greenwood_etal_2019. *GI*, *GIGANTEA*; LD, light-dark; LL, constant light; *LUC*, *LUCIFERASE*.
(TIF)

S2 Fig. Organs show similar clock phase and period differences under constant environmental conditions in multiple clock reporter lines. (A–C) Times of peaks of expression of *PRR9*::*LUC* (A), *TOC1*::*LUC* (B), or *ELF4*::*LUC* (C) in different organs under the LD-to-LL condition. Plots represent the 25th percentile, median, and the 75th percentile for the peak times of organs scored as rhythmic. $^{***}p < 0.001$, Kruskal-Wallis ANOVA. (D–F) Period estimates of *PRR9*::*LUC* (D), *TOC1*::*LUC* (E), or *ELF4*::*LUC* (F) expression for different organs imaged under the LD-to-LL condition. Box plots indicate the median and upper and lower quartiles, and whiskers the 9th and 91st percentiles of organs scored as rhythmic. For *PRR9*::*LUC*, $N = 3$; *TOC1*::*LUC*, $N = 3$; *ELF4*::*LUC*, $N = 3$. For all, $n = 11–18$. *N* represents the number of independent experiments and *n* the total number of organs tracked. See S1 and S2 Files for exact *n*, test statistics, and percentage rhythmicity of each organ. A subset of *PRR9*::*LUC* data is an analysis of time-lapse movies carried out in our previous work [5]. Underlying data are available from https://gitlab.com/slcu/teamJL/greenwood_etal_2019. *ELF4*, *EARLY FLOWERING 4*; LD, light-dark; LL, constant light; *LUC*, *LUCIFERASE*; *PRR9*, *PSEUDO-RESPONSE REGULATOR 9*; *TOC1*, *TIMING OF CAB EXPRESSION 1*.
(TIF)

S3 Fig. Organs show clock phase differences under LD cycles from the first to the final oscillation. Times of peaks of *GI*::*LUC* expression in different organs during the first (left) and final (right) observed oscillations under the LD-to-LD condition. Means are statistically different ($p < 0.05$, one-way ANOVA, Tukey post hoc tests) if they do not have a letter in common. *N* and *n* are as presented in Fig 2. *N* represents the number of independent experiments and *n* the total number of organs tracked. See S2 File for exact *n*, test statistics, and percentage

rhythmicity of each organ. Box plots indicate the median and upper and lower quartiles, and whiskers the 9th and 91st percentiles of organs scored as rhythmic. Underlying data are available from https://gitlab.com/slcu/teamJL/greenwood_etal_2019. *GI*, *GIGANTEA*; LD, light-dark; *LUC*, *LUCIFERASE*.
(TIF)

S4 Fig. Space-time phase plots from luciferase images. (A) Luciferase images are thresholded and a line fitted through the center of mass of the organ. At each index on this line, the normal line is taken. (B) Each normal line is rasterized and limited to 5 pixels around the center of mass to give pixel coordinates for longitudinal sections. (C) The mean value across longitudinal sections is taken at each time point to create a raw intensity space-time plot of a single seedling. (D) The phase of the oscillations is extracted using a wavelet transform to give a space-time map of the phase.
(TIF)

S5 Fig. Phase differences between organs following cuts is comparable to controls. (A-C) Times of peaks of *GI*::*LUC* expression in different organs for the first (left) and final (right) observed oscillations following a cut at the hypocotyl junction (A), root tip (B), or both the hypocotyl junction and root tip (C) conditions. $^{*}p < 0.05$, Wilcoxon rank-sum test. *N* and *n* are as in Fig 3. *N* represents the number of independent experiments and *n* the total number of organs tracked. See S2 File for exact *n*, test statistics, and percentage rhythmicity of each organ. Box plots indicate the median and upper and lower quartiles, and whiskers the 9th and 91st percentiles of organs scored as rhythmic. Underlying data are available from https://gitlab.com/slcu/teamJL/greenwood_etal_2019. *GI*, *GIGANTEA*; *LUC*, *LUCIFERASE*.
(TIF)

S6 Fig. Template for simulations with organ-specific periods and the ROI used for analysis. (A, B) Template for simulations, in which, in A, the periods of the pixels in each tissue are set to the mean periods measured in the LD-to-LL experimental data. In B, a representative set of periods for each region are shown, as drawn from the period distributions described in Materials and methods. (C, D) Template for simulations of the alternative model, in which, in C, periods of the pixels in each tissue are set to the mean periods measured in the LD-to-LL experimental data but with a gradient of periods in the root, as described in Materials and methods. In D, a representative set of seedling periods are shown, drawn from the period distributions and gradient described in Materials and methods. (E) The 5-by-5 pixel ROIs used for phase and period analyses are identified on the template. LD, light-dark; LL, constant light; ROI, region of interest.
(TIF)

S7 Fig. Phase plots for LD-to-LL simulations with increasing strengths of coupling. Phase plots of simulated *GI* expression across longitudinal sections of the hypocotyl and root. Each phase plot is a simulation of a single seedling, each with a different strength of coupling (*K*). *GI*, *GIGANTEA*; LD, light-dark; LL, constant light.
(TIF)

S8 Fig. The distribution of periods within a single seedling for simulations of the LD-to-LL condition with increasing strengths of coupling. The distribution of periods of simulated *GI* from individual pixels on the model template of a seedling is shown. Each plot shows the distribution for the simulation of a single seedling under the LD-to-LL condition with different

strengths of coupling (*K*). *GI*, *GIGANTEA*; LD, light-dark; LL, constant light; SD, standard deviation.
(TIF)

S9 Fig. The distribution of phases within a single seedling for simulations of the LD-to-LL condition with increasing strengths of coupling. The distribution of phases of simulated *GI* from individual pixels on the model template of a seedling is shown. Each plot shows the distribution for the simulation of a single seedling under the LD-to-LL condition with different strengths of coupling (*K*). *GI*, *GIGANTEA*; LD, light-dark; LL, constant light; SD, standard deviation.
(TIF)

S10 Fig. Phase plots for alternative model simulations with differing spatial structure of periods. (A, B) Phase plot of simulated *GI* expression across longitudinal sections of the hypocotyl and root of a single seedling for the LL-to-LL condition in the absence of coupling ($K = 0$), but with period differences. In A, periods of the pixels in each tissue are set to the mean periods measured in the LD-to-LL experimental data, without noise ($\Omega = 0$). In B, a representative set of periods for each region are shown, as drawn from the period distributions described in Materials and methods ($\Omega = 0.1$). (C, D) Phase plot of simulated *GI* expression across longitudinal sections of the hypocotyl and root of a single seedling for the LD-to-LL condition in the absence of coupling ($K = 0$). In C, periods in the root region are graded with a maximum period in the middle of the root, without noise ($\Omega = 0$). In D, periods are also graded in the root, but periods are drawn from a distribution ($\Omega = 0.1$). See Materials and methods for details. (E, F) Phase plot of simulated *GI* expression across longitudinal sections of the hypocotyl and root of a single seedling for the LL-to-LL condition in the absence of coupling ($K = 0$). In E, periods in the root region are graded with a maximum period in the middle of the root, without noise ($\Omega = 0$). In F, periods are also graded in the root, but periods are drawn from a distribution ($\Omega = 0.1$). See Materials and methods for details. *GI*, *GIGANTEA*; LD, light-dark; LL, constant light.
(TIF)

S11 Fig. Representative phase plots for the LL-to-LL condition. Phase plots of *GI*::*LUC* expression across longitudinal sections of the hypocotyl and root. Each phase plot is of a single seedling that is representative for the LL-to-LL condition. *N* and *n* are as presented in Fig 5. *N* represents the number of independent experiments and *n* the total number of organs tracked. See S1 or S2 Files for exact *n* and percentage rhythmicity. *GI*, *GIGANTEA*; LL, constant light; *LUC*, *LUCIFERASE*.
(TIF)

S12 Fig. Core clock network mutations effect the period of different regions proportionately. (A) Period estimates for *GI*::*LUC* expression from different organs imaged under the LD-to-LL condition in circadian mutant lines. (B) Period change relative to the cotyledon for *GI*::*LUC* expression from different organs imaged under the LD-to-LL condition in circadian mutant lines. For *cca1-11*, $N = 4$; *prr7-3*, $N = 4$; *prr9-1*, $N = 2$; *toc1-101*, $N = 2$; *lux-4*, $N = 2$. For all, $n = 5–18$. *N* represents the number of independent experiments and *n* the total number of organs tracked. See S1 File for exact *n*, test statistics, and percentage rhythmicity of each organ. Box plots indicate the median and upper and lower quartiles, and whiskers the 9th and 91st percentiles of organs scored as rhythmic. Individual data points are shown when the number of rhythmic plants is less than five. Horizontal position of scatter points is for clarity and has no meaning. Underlying data are available from

https://gitlab.com/slcu/teamJL/greenwood_etal_2019. *GI*, *GIGANTEA*; LD, light-dark; LL, constant light; *LUC*, *LUCIFERASE*.
(TIF)

S13 Fig. Phase shifts between aerial organs and the root are reduced under DD. Times of peaks of *GI*::*LUC* expression in different organs during the first (left) and final (right) observed oscillations under DD. Means are statistically different ($p < 0.05$, one-way ANOVA, Tukey post hoc tests) if they do not have a letter in common. *N* and *n* are as presented in Fig 6. *N* represents the number of independent experiments and *n* the total number of organs tracked. See S2 File for exact *n*, test statistics, and percentage rhythmicity of each organ. Box plots indicate the median and upper and lower quartiles, and whiskers the 9th and 91st percentiles of organs scored as rhythmic. Underlying data are available from https://gitlab.com/slcu/teamJL/greenwood_etal_2019. DD, constant darkness. *GI*, *GIGANTEA*; *LUC*, *LUCIFERASE*.
(TIF)

S14 Fig. Exposing roots to light during entrainment has minimal effects on circadian dynamics observed during imaging. (A) Seeds are sown on agar-filled black micro-centrifuge tube lids with a piercing in the lid (left), and suspended in MS liquid in a floating micro-centrifuge tube rack (right), as described previously [88]. Seedlings are entrained for 4 d, with the roots either exposed to light or kept in the dark using this system. Seedlings are then imaged under DD. Note that images include a blur selectively on the background in order to highlight these components. (B) Period estimates of *GI*::*LUC* expression for the different organs when roots are exposed to light during entrainment or when kept in the dark. All comparisons between period estimates are not significant, $p < 0.05$, by two-tailed *t* test, Welch correction. Box plots indicate the median and upper and lower quartiles, and whiskers the 9th and 91st percentiles of organs scored as rhythmic. (C) Times of peaks of *GI*::*LUC* expression for the different organs presented in B. Plots represent the 25th percentile, median, and the 75th percentile for the peak times of organs scored as rhythmic. $N = 3$; $n = 14–15$. *N* represents the number of independent experiments and *n* the total number of organs tracked. See S1 and S2 Files for exact *n*, test statistics, and percentage rhythmicity of each organ. Underlying data are available from https://gitlab.com/slcu/teamJL/greenwood_etal_2019. DD, constant darkness; *GI*, *GIGANTEA*; *LUC*, *LUCIFERASE*; MS, Murashige and Skoog.
(TIF)

S15 Fig. The wavelength of light influences the clock in an organ-specific manner. (A, B) Period estimates of *GI*::*LUC* expression for different organs under constant red and blue light, plotted against red-light-only (A) or blue-light-only data (B). $^{***}p < 0.001$, two-tailed *t* test, Welch correction. Box plots indicate the median and upper and lower quartiles, and whiskers the 9th and 91st percentiles of organs scored as rhythmic. (C, D) Times of peaks of *GI*::*LUC* expression in different organs imaged under constant red and blue light, plotted against constant red (C) or constant blue light data (D). Plots represent the 25th percentile, median, and the 75th percentile for the peak times of organs scored as rhythmic. For red and blue light data, *N* and *n* are as presented in Fig 2. For constant red light, $N = 2$; constant blue light, $N = 2$. For both, $n = 22–25$. *N* represents the number of independent experiments and *n* the total number of organs tracked. See S1 and S2 Files for exact *n*, test statistics, and percentage rhythmicity in each organ. Constant blue light data are an analysis of time-lapse movies we carried out in previous work [5]. Underlying data are available from https://gitlab.com/slcu/teamJL/greenwood_etal_2019. *GI*, *GIGANTEA*; *LUC*, *LUCIFERASE*.
(TIF)

S16 Fig. *PHYB* sets clock periods organ specifically under constant red light and DD. (A) Times of peaks of *GI*::*LUC* expression in different organs during the first (left) and final (right) observed oscillations in the *phyb-9* mutant imaged under constant red light. Means are statistically different ($p < 0.05$, one-way ANOVA, Tukey post hoc tests) if they do not have a letter in common. (B) Period estimates of *GI*::*LUC* expression for different organs in the *phyb-9* mutant imaged under DD. $^{*}p < 0.05$, two-tailed *t* test, Welch correction. Box plots indicate the median and upper and lower quartiles, and whiskers the 9th and 91st percentiles of organs scored as rhythmic. (C) Times of peaks of *GI*::*LUC* expression in different organs in the *phyb-9* mutant imaged under DD. For *phyb-9* red light, *N* and *n* are as presented in Fig 6; *phyb-9* DD, $N = 2$, $n = 17–18$. *N* represents the number of independent experiments and *n* the total number of organs tracked. See S1 and S2 Files for exact *n*, test statistics, and percentage rhythmicity of each organ. Plots represent the 25th percentile, median, and the 75th percentile for the peak times of organs scored as rhythmic. Underlying data are available from https://gitlab.com/slcu/teamJL/greenwood_etal_2019. DD, constant darkness; *GI*, *GIGANTEA*; *LUC*, *LUCIFERASE*; *PHYB*, *PHYTOCHROME B*.
(TIF)

S17 Fig. Phase shifts between aerial organs and the root are reduced following the inhibition of photosynthesis by DCMU. Times of peaks of *GI*::*LUC* expression in different organs during the first (left) and final (right) observed oscillations during the inhibition of photosynthesis by DCMU. Means are statistically different ($p < 0.05$, one-way ANOVA, Tukey post hoc tests) if they do not have a letter in common. *N* and *n* are as presented in Fig 7. *N* represents the number of independent experiments and *n* the total number of organs tracked. See S2 File for exact *n*, test statistics, and percentage rhythmicity of each organ. Box plots indicate the median and upper and lower quartiles, and whiskers the 9th and 91st percentiles of organs scored as rhythmic. Underlying data are available from https://gitlab.com/slcu/teamJL/greenwood_etal_2019. DCMU, 3-(3,4-dichlorophenyl)-1,1-dimethylurea; *GI*, *GIGANTEA*; *LUC*, *LUCIFERASE*.
(TIF)

S18 Fig. The application of sugar to the top of the root creates a phase shift from the top to the middle of the root under DD. (A) Times of peaks of *GI*::*LUC* expression in different regions during the first (left) and final (right) observed oscillations during the partial contact of the root with sucrose. $^{***}p < 0.001$, Wilcoxon rank-sum test. (B) Times of peaks of expression in different regions during the first (left) and final (right) observed oscillations during the partial contact of the root with mannitol. $^{**}p < 0.01$, Wilcoxon rank-sum test. *N* and *n* are as presented in Fig 7. *N* represents the number of independent experiments and *n* the total number of organs tracked. See S2 File for exact *n*, test statistics, and percentage rhythmicity of each organ. Box plots indicate the median and upper and lower quartiles, and whiskers the 9th and 91st percentiles of organs scored as rhythmic. Underlying data are available from https://gitlab.com/slcu/teamJL/greenwood_etal_2019. DD, constant darkness; *GI*, *GIGANTEA*; *LUC*, *LUCIFERASE*.
(TIF)

S1 Video. Spatial waves of *GI*::*LUC* expression under the LD-to-LL condition. *GI*::*LUC* luminescence from 24 to 144 h after transfer to LL. Frame intervals are 90 min and the scale bar shows 0.5 mm. *GI*, *GIGANTEA*; LD, light-dark; LL, constant light; *LUC*, *LUCIFERASE*.
(MP4)

S2 Video. Spatial waves of *GI*::*LUC* expression under the LD-to-LD condition. *GI*::*LUC* luminescence from 120 to 240 h under LD cycles. Frame intervals are 90 min and the scale bar shows 0.5 mm. *GI*, *GIGANTEA*; LD, light-dark; *LUC*, *LUCIFERASE*.
(MP4)

S3 Video. Spatial waves of *GI*::*LUC* expression in a cut root. *GI*::*LUC* luminescence from 24 to 144 h after transfer to LL, following excision of the root tip 2 h after transfer to LL. Frame intervals are 90 min and the scale bar shows 0.5 mm. *GI*, *GIGANTEA*; LL, constant light; *LUC*, *LUCIFERASE*.
(MP4)

S4 Video. Spatial waves of *GI*::*LUC* expression under the LL-to-LL condition. *GI*::*LUC* luminescence from 120 to 240 h after transfer to LL. Frame intervals are 90 min and the scale bar shows 0.5 mm. *GI*, *GIGANTEA*; LL, constant light; *LUC*, *LUCIFERASE*.
(MP4)

S5 Video. Spatial waves of *GI*::*LUC* expression under DD. *GI*::*LUC* luminescence from 24 to 144 h after transfer to DD. Frame intervals are 90 min and the scale bar shows 0.5 mm. DD, constant darkness; *GI*, *GIGANTEA*; *LUC*, *LUCIFERASE*.
(MP4)

S6 Video. Spatial waves of *GI*::*LUC* expression under constant red light in the *phyb-9* background. *GI*::*LUC* luminescence from 24 to 144 h after transfer to DD. Frame intervals are 90 min and the scale bar shows 0.5 mm. DD, constant darkness; *GI*, *GIGANTEA*; *LUC*, *LUCIFERASE*.
(MP4)

S7 Video. Spatial waves of *GI*::*LUC* expression in the root following application of exogenous sucrose to the top of the root. *GI*::*LUC* luminescence from 24 to 144 h after transfer to DD. The top portion of the root (approximately 1 mm) is in contact with sucrose-supplemented media, whilst the remainder of the root is in contact with media without sugar. Frame intervals are 90 min and the scale bar shows 0.5 mm. DD, constant darkness; *GI*, *GIGANTEA*; *LUC*, *LUCIFERASE*.
(MP4)

S8 Video. Spatial waves of *GI*::*LUC* expression in the root following application of exogenous mannitol to the top of the root. *GI*::*LUC* luminescence from 24 to 144 h after transfer to DD. The top portion of the root (approximately 1 mm) is in contact with mannitol-supplemented media, whilst the remainder of the root is in contact with media without sugar. Frame intervals are 90 min and the scale bar shows 0.5 mm. DD, constant darkness; *GI*, *GIGANTEA*; *LUC*, *LUCIFERASE*.
(MP4)

S1 File. Statistic values relating to period estimates presented in the figures. *N*, *n*, rhythmicity scores, and test statistics for the periods presented in all figures. Values are separated by sheet, each corresponding to the data presented in one or more of the figures.
(XLSX)

S2 File. Statistic values relating to phase estimates presented in the figures. *N*, *n*, rhythmicity scores, and test statistics for the phases presented in all figures. Values are separated by sheet, each corresponding to the data presented in one or more of the figures.
(XLSX)

Acknowledgments

We thank Professor Alex Webb (University of Cambridge), Dr. Katie Abley (University of Cambridge), Dr. Susan Duncan (Earlham Institute), and Dr. Ozgur Akman (University of Exeter) for critical reading of the manuscript and Dr. Laszlo Kozma-Bognar (Hungarian Academy of Sciences) for gifts of transgenic material. We also thank contributors to the Plant Illustrations Repository [101] for a graphic utilized in Fig 1.

Author Contributions

Conceptualization: Anthony J. W. Hall, James C. W. Locke.

Data curation: Mark Greenwood.

Formal analysis: Mark Greenwood, Mirela Domijan.

Funding acquisition: James C. W. Locke.

Investigation: Mark Greenwood, Mirela Domijan.

Methodology: Mark Greenwood, Mirela Domijan, Anthony J. W. Hall.

Project administration: James C. W. Locke.

Resources: Peter D. Gould, Anthony J. W. Hall.

Software: Mark Greenwood, Mirela Domijan.

Supervision: Anthony J. W. Hall, James C. W. Locke.

Validation: Mirela Domijan.

Visualization: Mark Greenwood.

Writing – original draft: Mark Greenwood, James C. W. Locke.

Writing – review & editing: Mirela Domijan, Anthony J. W. Hall, James C. W. Locke.

References

1. Bell-Pedersen D, Cassone VM, Earnest DJ, Golden SS, Hardin PE, Thomas TL, et al. Circadian rhythms from multiple oscillators: lessons from diverse organisms. Nat Rev Genet. 2005 Jul 10; 6 (7):544–56. https://doi.org/10.1038/nrg1633 PMID: 15951747
2. McClung CR. Plant circadian rhythms. Plant Cell. 2006 Apr 1; 18(4):792–803. https://doi.org/10.1105/tpc.106.040980 PMID: 16595397
3. Endo M. Tissue-specific circadian clocks in plants. Curr Opin Plant Biol. 2016 Feb; 29:44–9. https://doi.org/10.1016/j.pbi.2015.11.003 PMID: 26723003
4. Para A, Farré EM, Imaizumi T, Pruneda-Paz JL, Harmon FG, Kay SA. PRR3 Is a vascular regulator of TOC1 stability in the Arabidopsis circadian clock. Plant Cell. 2007 Nov 1; 19(11):3462–73. https://doi.org/10.1105/tpc.107.054775 PMID: 18055606
5. Gould PD, Domijan M, Greenwood M, Tokuda IT, Rees H, Kozma-Bognar L, et al. Coordination of robust single cell rhythms in the Arabidopsis circadian clock via spatial waves of gene expression. Elife. 2018 Apr 26; 7:e31700. https://doi.org/10.7554/eLife.31700 PMID: 29697372
6. Bordage S, Sullivan S, Laird J, Millar AJ, Nimmo HG. Organ specificity in the plant circadian system is explained by different light inputs to the shoot and root clocks. New Phytol. 2016 Oct; 212(1):136–49. https://doi.org/10.1111/nph.14024 PMID: 27240972
7. Koo J, Kim Y, Kim J, Yeom M, Lee IC, Nam HG. A GUS/Luciferase Fusion Reporter for Plant Gene Trapping and for Assay of Promoter Activity with Luciferin-Dependent Control of the Reporter Protein Stability. Plant Cell Physiol. 2007 Aug 1; 48(8):1121–31. https://doi.org/10.1093/pcp/pcm081 PMID: 17597079
8. Edwards J, Martin AP, Andriunas F, Offler CE, Patrick JW, McCurdy DW. GIGANTEA is a component of a regulatory pathway determining wall ingrowth deposition in phloem parenchyma transfer cells of

Arabidopsis thaliana. Plant J. 2010 Aug; 63(4):651–61. https://doi.org/10.1111/j.1365-313X.2010.04269.x PMID: 20545890

9. Lee HG, Seo PJ. Dependence and independence of the root clock on the shoot clock in Arabidopsis. Genes Genomics. 2018 Jun 13;1–6.
10. Endo M, Shimizu H, Nohales MA, Araki T, Kay SA. Tissue-specific clocks in Arabidopsis show asymmetric coupling. Nature. 2014 Oct 29; 515:419–22. https://doi.org/10.1038/nature13919 PMID: 25363766
11. Shimizu H, Katayama K, Koto T, Torii K, Araki T, Endo M. Decentralized circadian clocks process thermal and photoperiodic cues in specific tissues. Nat Plants. 2015 Nov 2; 1(11):15163.
12. Shimizu H, Araki T, Endo M. Photoperiod sensitivity of the Arabidopsis circadian clock is tissue-specific. Plant Signal Behav. 2015; 10(6):e1010933. https://doi.org/10.1080/15592324.2015.1010933 PMID: 26176897
13. Michael TP, Salome PA, McClung CR. Two Arabidopsis circadian oscillators can be distinguished by differential temperature sensitivity. Proc Natl Acad Sci U S A. 2003 May 27; 100(11):6878–83. https://doi.org/10.1073/pnas.1131995100 PMID: 12736379
14. Brown SA, Azzi A. Peripheral Circadian Oscillators in Mammals. In Springer, Berlin, Heidelberg; 2013. p. 45–66.
15. Balsalobre A, Damiola F, Schibler U. A serum shock induces circadian gene expression in mammalian tissue culture cells. Cell. 1998 Jun 12; 93(6):929–37. https://doi.org/10.1016/s0092-8674(00)81199-x PMID: 9635423
16. Balsalobre A. Clock genes in mammalian peripheral tissues. Cell Tissue Res. 2002 Jul 24; 309 (1):193–9. https://doi.org/10.1007/s00441-002-0585-0 PMID: 12111549
17. Pett JP, Kondoff M, Bordyugov G, Kramer A, Herzel H. Co-existing feedback loops generate tissue-specific circadian rhythms. Life Sci alliance. 2018 Jun 1; 1(3):e201800078. https://doi.org/10.26508/lsa.201800078 PMID: 30456356
18. Wenden B, Toner DLK, Hodge SK, Grima R, Millar AJ. Spontaneous spatiotemporal waves of gene expression from biological clocks in the leaf. Proc Natl Acad Sci U S A. 2012 Apr 24; 109(17):6757–62. https://doi.org/10.1073/pnas.1118814109 PMID: 22496591
19. Fukuda H, Nakamichi N, Hisatsune M, Murase H, Mizuno T. Synchronization of Plant Circadian Oscillators with a Phase Delay Effect of the Vein Network. Phys Rev Lett. 2007 Aug; 99(9):098102. https://doi.org/10.1103/PhysRevLett.99.098102 PMID: 17931039
20. Fukuda H, Ukai K, Oyama T. Self-arrangement of cellular circadian rhythms through phase-resetting in plant roots. Phys Rev E. 2012 Oct; 86(4):041917.
21. Muranaka T, Oyama T. Heterogeneity of cellular circadian clocks in intact plants and its correction under light-dark cycles. Sci Adv. 2016 Jul 15; 2(7):e1600500–e1600500. https://doi.org/10.1126/sciadv.1600500 PMID: 27453946
22. Takahashi N, Hirata Y, Aihara K, Mas P. A Hierarchical Multi-oscillator Network Orchestrates the Arabidopsis Circadian System. Cell. 2015 Sep; 163(1):148–59. https://doi.org/10.1016/j.cell.2015.08.062 PMID: 26406375
23. Yakir E, Hassidim M, Melamed-Book N, Hilman D, Kron I, Green RM. Cell autonomous and cell-type specific circadian rhythms in Arabidopsis. Plant J. 2011 Nov; 68(3):520–31. https://doi.org/10.1111/j.1365-313X.2011.04707.x PMID: 21781194
24. James AB, Monreal JA, Nimmo GA, Kelly CL, Herzyk P, Jenkins GI, et al. The circadian clock in Arabidopsis roots is a simplified slave version of the clock in shoots. Science. 2008 Dec 19; 322 (5909):1832–5. https://doi.org/10.1126/science.1161403 PMID: 19095940
25. Rascher U, Hütt MT, Siebke K, Osmond B, Beck F, Lüttge U. Spatiotemporal variation of metabolism in a plant circadian rhythm: the biological clock as an assembly of coupled individual oscillators. Proc Natl Acad Sci U S A. 2001 Sep 25; 98(20):11801–5. https://doi.org/10.1073/pnas.191169598 PMID: 11573013
26. Ukai K, Inai K, Nakamichi N, Ashida H, Yokota A, Hendrawan Y, et al. Traveling Waves of Circadian Gene Expression in Lettuce. Environ Control Biol. 2012 Oct 30; 50(3):237–46.
27. Ukai K, Murase H, Fukuda H. Spatiotemporal dynamics of circadian clock in lettuce. IFAC Proc Vol. 2013 Jan 1; 46(4):214–7.
28. Nimmo HG. Entrainment of Arabidopsis roots to the light:dark cycle by light piping. Plant Cell Environ. 2018 Aug 1; 41(8):1742–8. https://doi.org/10.1111/pce.13137 PMID: 29314066
29. Bloemendal S, Kück U. Cell-to-cell communication in plants, animals, and fungi: a comparative review. Naturwissenschaften. 2013 Jan 6; 100(1):3–19. https://doi.org/10.1007/s00114-012-0988-z PMID: 23128987

30. Park DH, Somers DE, Kim YS, Choy YH, Lim HK, Soh MS, et al. Control of circadian rhythms and photoperiodic flowering by the Arabidopsis GIGANTEA gene. Science. 1999; 285(5433):1579–82. https://doi.org/10.1126/science.285.5433.1579 PMID: 10477524

31. Ito S, Matsushika A, Yamada H, Sato S, Kato T, Tabata S, et al. Characterization of the APRR9 pseudo-response regulator belonging to the APRR1/TOC1 quintet in Arabidopsis thaliana. Plant Cell Physiol. 2003 Nov; 44(11):1237–45. https://doi.org/10.1093/pcp/pcg136 PMID: 14634162

32. Millar AJ, Carre IA, Strayer CA, Chua NH, Kay SA. Circadian clock mutants in Arabidopsis identified by luciferase imaging. Science. 1995; 267:1161–3. https://doi.org/10.1126/science.7855595 PMID: 7855595

33. Doyle MR, Davis SJ, Bastow RM, McWatters HG, Kozma-Bognár L, Nagy F, et al. The ELF4 gene controls circadian rhythms and flowering time in Arabidopsis thaliana. Nature. 2002 Sep 5; 419 (6902):74–7. https://doi.org/10.1038/nature00954 PMID: 12214234

34. Pittendrigh CS. Circadian Systems: Entrainment. In: Biological Rhythms. Boston, MA: Springer US; 1981. p. 95–124.

35. Granada AE, Bordyugov G, Kramer A, Herzel H. Human chronotypes from a theoretical perspective. PLoS One. 2013; 8(3):e59464. https://doi.org/10.1371/journal.pone.0059464 PMID: 23544070

36. Bordyugov G, Abraham U, Granada A, Rose P, Imkeller K, Kramer A, et al. Tuning the phase of circadian entrainment. J R Soc Interface. 2015 Jul 6; 12(108):20150282. https://doi.org/10.1098/rsif.2015.0282 PMID: 26136227

37. Kuramoto Y. Self-entrainment of a population of coupled non-linear oscillators. In: International Symposium on Mathematical Problems in Theoretical Physics. Berlin/Heidelberg: Springer-Verlag; 1975. p. 420–2.

38. Schmal C, Herzog ED, Herzel H. Measuring Relative Coupling Strength in Circadian Systems. J Biol Rhythms. 2018;

39. Aschoff J, Pohl H. Phase relations between a circadian rhythm and its zeitgeber within the range of entrainment. Naturwissenschaften. 1978 Feb; 65(2):80–4. PMID: 345129

40. Dodd AN, Dalchau N, Gardner MJ, Baek S-J, Webb AAR. The circadian clock has transient plasticity of period and is required for timing of nocturnal processes in Arabidopsis. New Phytol. 2014 Jan; 201 (1):168–79. https://doi.org/10.1111/nph.12489 PMID: 24102325

41. Edwards KD, Akman OE, Knox K, Lumsden PJ, Thomson AW, Brown PE, et al. Quantitative analysis of regulatory flexibility under changing environmental conditions. Mol Syst Biol. 2010 Nov 2; 6(1):424.

42. Winfree AT. The geometry of biological time. Springer-Verlag; 1960. 530 p.

43. Kuramoto Y. Chemical Oscillations, Waves, and Turbulence. Berlin, Heidelberg: Springer Berlin Heidelberg; 1984. (Springer Series in Synergetics; vol. 19).

44. Sakaguchi H. Cooperative Phenomena in Coupled Oscillator Systems under External Fields. Prog Theor Phys. 1988 Jan 1; 79(1):39–46.

45. Gonze D, Bernard S, Waltermann C, Kramer A, Herzel H. Spontaneous synchronization of coupled circadian oscillators. Biophys J. 2005 Jul; 89(1):120–9. https://doi.org/10.1529/biophysj.104.058388 PMID: 15849258

46. Seki N, Tanigaki Y, Yoshida A, Fukuda H. Spatiotemporal Analysis of Localized Circadian Arrhythmias in Plant Roots. Environ Control Biol. 2018; 56(3):93–7.

47. Zhong HH, Painter JE, Salomé PA, Straume M, McClung CR. Imbibition, but not release from stratification, sets the circadian clock in Arabidopsis seedlings. Plant Cell. 1998 Dec; 10(12):2005–17. https://doi.org/10.1105/tpc.10.12.2005 PMID: 9836741

48. Salomé PA, Xie Q, McClung CR, Hangarter RP, McClung CR. Circadian timekeeping during early Arabidopsis development. Plant Physiol. 2008 Jul 1; 147(3):1110–25. https://doi.org/10.1104/pp.108.117622 PMID: 18480377

49. Whitelam GC, Devlin PF. Roles of different phytochromes in Arabidopsis photomorphogenesis. Plant, Cell Environ. 1997 Jun 1; 20(6):752–8.

50. Sharrock RA, Quail PH. Novel phytochrome sequences in Arabidopsis thaliana: structure, evolution, and differential expression of a plant regulatory photoreceptor family. Genes Dev. 1989 Nov; 3 (11):1745–57. https://doi.org/10.1101/gad.3.11.1745 PMID: 2606345

51. Somers DE, Quail PH. Phytochrome-Mediated Light Regulation of PHYA- and PHYB-GUS Transgenes in Arabidopsis thaliana Seedlings. Plant Physiol. 1995 Feb; 107(2):523–34. https://doi.org/10.1104/pp.107.2.523 PMID: 12228380

52. Somers DE, Quail PH. Temporal and spatial expression patterns of PHYA and PHYB genes in Arabidopsis. Plant J. 1995 Mar 1; 7(3):413–27. PMID: 7757114

53. Bognár LK, Hall A, Adám E, Thain SC, Nagy F, Millar AJ. The circadian clock controls the expression pattern of the circadian input photoreceptor, phytochrome B. Proc Natl Acad Sci U S A. 1999 Dec 7; 96 (25):14652–7. https://doi.org/10.1073/pnas.96.25.14652 PMID: 10588760

54. Tóth R, Kevei E, Hall A, Millar AJ, Nagy F, Kozma-Bognár L. Circadian clock-regulated expression of phytochrome and cryptochrome genes in Arabidopsis. Plant Physiol. 2001 Dec; 127(4):1607–16. https://doi.org/10.1104/pp.010467 PMID: 11743105

55. Somers DE, Devlin PF, Kay SA. Phytochromes and cryptochromes in the entrainment of the Arabidopsis circadian clock. Science. 1998 Nov 20; 282(5393):1488–90. https://doi.org/10.1126/science.282.5393.1488 PMID: 9822379

56. Sanchez SE, Kay SA. The Plant Circadian Clock: From a Simple Timekeeper to a Complex Developmental Manager. Cold Spring Harb Perspect Biol. 2016 Sep 23;a027748.

57. Dalchau N, Baek SJ, Briggs HM, Robertson FC, Dodd AN, Gardner MJ, et al. The circadian oscillator gene GIGANTEA mediates a long-term response of the Arabidopsis thaliana circadian clock to sucrose. Proc Natl Acad Sci U S A. 2011 Mar 22; 108(12):5104–9. https://doi.org/10.1073/pnas.1015452108 PMID: 21383174

58. Haydon MJ, Mielczarek O, Robertson FC, Hubbard KE, Webb AAR. Photosynthetic entrainment of the Arabidopsis thaliana circadian clock. Nature. 2013 Oct 31; 502(7473):689–92. https://doi.org/10.1038/nature12603 PMID: 24153186

59. Frank A, Matiolli CC, Viana AJC, Hearn TJ, Kusakina J, Belbin FE, et al. Circadian Entrainment in Arabidopsis by the Sugar-Responsive Transcription Factor bZIP63. Curr Biol. 2018 Aug 20; 28(16):2597–2606.e6. https://doi.org/10.1016/j.cub.2018.05.092 PMID: 30078562

60. Oyama T, Shimura Y, Okada K. The Arabidopsis HY5 gene encodes a bZIP protein that regulates stimulus-induced development of root and hypocotyl. Genes Dev. 1997 Nov 15; 11(22):2983–95. https://doi.org/10.1101/gad.11.22.2983 PMID: 9367981

61. Chen X, Yao Q, Gao X, Jiang C, Harberd NP, Fu X. Shoot-to-Root Mobile Transcription Factor HY5 Coordinates Plant Carbon and Nitrogen Acquisition. Curr Biol. 2016 Mar 7; 26(5):640–6. https://doi.org/10.1016/j.cub.2015.12.066 PMID: 26877080

62. Lee H-J, Ha J-H, Kim S-G, Choi H-K, Kim ZH, Han Y-J, et al. Stem-piped light activates phytochrome B to trigger light responses in Arabidopsis thaliana roots. Sci Signal. 2016 Nov 1; 9(452):ra106.

63. Li G, Siddiqui H, Teng Y, Lin R, Wan X, Li J, et al. Coordinated transcriptional regulation underlying the circadian clock in Arabidopsis. Nat Cell Biol. 2011 May 17; 13(5):616–22. https://doi.org/10.1038/ncb2219 PMID: 21499259

64. Andronis C, Barak S, Knowles SM, Sugano S, Tobin EM. The Clock Protein CCA1 and the bZIP Transcription Factor HY5 Physically Interact to Regulate Gene Expression in Arabidopsis. Mol Plant. 2008 Jan; 1(1):58–67. https://doi.org/10.1093/mp/ssm005 PMID: 20031914

65. Hajdu A, Dobos O, Domijan M, Bálint B, Nagy I, Nagy F, et al. ELONGATED HYPOCOTYL 5 mediates blue light signalling to the Arabidopsis circadian clock. Plant J. 2018 Dec 1; 96(6):1242–54. https://doi.org/10.1111/tpj.14106 PMID: 30256479

66. Thieme CJ, Rojas-Triana M, Stecyk E, Schudoma C, Zhang W, Yang L, et al. Endogenous Arabidopsis messenger RNAs transported to distant tissues. Nat Plants. 2015 Mar 23; 1(4):15025. https://doi.org/10.1038/nplants.2015.25 PMID: 27247031

67. Libault M, Pingault L, Zogli P, Schiefelbein J. Plant Systems Biology at the Single-Cell Level. Trends Plant Sci. 2017 Nov 1; 22(11):949–60. https://doi.org/10.1016/j.tplants.2017.08.006 PMID: 28970001

68. Duncan S, Rosa S. Gaining insight into plant gene transcription using smFISH. Transcription. 2018 May 27; 9(3):166–70. https://doi.org/10.1080/21541264.2017.1372043 PMID: 28990856

69. Dawson GB, Fisher RG. Diurnal and seasonal ground temperature variations at Wairakei. New Zeal J Geol Geophys. 1964 Feb; 7(1):144–54.

70. Ahrens C. Meteorology today: An introduction to weather, climate, and the environment. Meteorology today: An introduction to weather, climate, and the environment. Pacific Grove, California: Thomson/Brooks/Cole; 2003. 64–66 p.

71. Shimizu H, Araki T, Endo M. Photoperiod sensitivity of the Arabidopsis circadian clock is tissue-specific. Plant Signal Behav. 2015; 10(6):e1010933. https://doi.org/10.1080/15592324.2015.1010933 PMID: 26176897

72. Yamaguchi S, Isejima H, Matsuo T, Okura R, Yagita K, Kobayashi M, et al. Synchronization of cellular clocks in the suprachiasmatic nucleus. Science. 2003 Nov 21; 302(5649):1408–12. https://doi.org/10.1126/science.1089287 PMID: 14631044

73. Welsh DK, Takahashi JS, Kay SA. Suprachiasmatic Nucleus: Cell Autonomy and Network Properties. Annu Rev Physiol. 2010 Mar 17; 72(1):551–77.

74. Fukuda H, Tokuda I, Hashimoto S, Hayasaka N, Hayashi S. Quantitative Analysis of Phase Wave of Gene Expression in the Mammalian Central Circadian Clock Network. PLoS ONE. 2011; 6(8):e23568. https://doi.org/10.1371/journal.pone.0023568 PMID: 21912598

75. Cortijo S, Aydin Z, Ahnert S, Locke JC. Widespread inter-individual gene expression variability in Arabidopsis thaliana. Mol Syst Biol. 2019 Jan 24; 15(1):e8591. https://doi.org/10.15252/msb.20188591 PMID: 30679203

76. Araújo IS, Pietsch JM, Keizer EM, Greese B, Balkunde R, Fleck C, et al. Stochastic gene expression in Arabidopsis thaliana. Nat Commun. 2017 Dec 14; 8(1):2132. https://doi.org/10.1038/s41467-017-02285-7 PMID: 29242599

77. Webb AAR, Seki M, Satake A, Caldana C. Continuous dynamic adjustment of the plant circadian oscillator. Nat Commun. 2019 Dec 1; 10(1):550. https://doi.org/10.1038/s41467-019-08398-5 PMID: 30710080

78. Hearn TJ, Marti Ruiz MC, Abdul-Awal SM, Wimalasekera R, Stanton CR, Haydon MJ, et al. BIG Regulates Dynamic Adjustment of Circadian Period in Arabidopsis thaliana. Plant Physiol. 2018 Sep 1; 178 (1):358–71. https://doi.org/10.1104/pp.18.00571 PMID: 29997180

79. Abraham U, Granada AE, Westermark PO, Heine M, Kramer A, Herzel H. Coupling governs entrainment range of circadian clocks. Mol Syst Biol. 2010 Nov 30; 6:438. https://doi.org/10.1038/msb.2010.92 PMID: 21119632

80. Palágyi A, Terecskei K, Adám E, Kevei E, Kircher S, Mérai Z, et al. Functional analysis of amino-terminal domains of the photoreceptor phytochrome B. Plant Physiol. 2010 Aug; 153(4):1834–45. https://doi.org/10.1104/pp.110.153031 PMID: 20530216

81. Locke JCW, Kozma-Bognár L, Gould PD, Fehér B, Kevei E, Nagy F, et al. Experimental validation of a predicted feedback loop in the multi-oscillator clock of Arabidopsis thaliana. Mol Syst Biol. 2006 Jan; 2:59. https://doi.org/10.1038/msb4100102 PMID: 17102804

82. Palágyi A, Terecskei K, Adám E, Kevei E, Kircher S, Mérai Z, et al. Functional analysis of amino-terminal domains of the photoreceptor phytochrome B. Plant Physiol. 2010 Aug; 153(4):1834–45. https://doi.org/10.1104/pp.110.153031 PMID: 20530216

83. Clough SJ, Bent AF. Floral dip: a simplified method for Agrobacterium-mediated transformation of Arabidopsis thaliana. Plant J. 1998 Dec; 16(6):735–43. PMID: 10069079

84. Hall A, Bastow RM, Davis SJ, Hanano S, McWatters HG, Hibberd V, et al. The TIME FOR COFFEE gene maintains the amplitude and timing of Arabidopsis circadian clocks. Plant Cell. 2003 Nov; 15 (11):2719–29. https://doi.org/10.1105/tpc.013730 PMID: 14555691

85. Farré EM, Harmer SL, Harmon FG, Yanovsky MJ, Kay SA. Overlapping and distinct roles of PRR7 and PRR9 in the Arabidopsis circadian clock. Curr Biol. 2005 Jan 11; 15(1):47–54. https://doi.org/10.1016/j.cub.2004.12.067 PMID: 15649364

86. Kikis EA, Khanna R, Quail PH. ELF4 is a phytochrome-regulated component of a negative-feedback loop involving the central oscillator components CCA1 and LHY. Plant J. 2005 Sep 12; 44(2):300–13. https://doi.org/10.1111/j.1365-313X.2005.02531.x PMID: 16212608

87. Hazen SP, Schultz TF, Pruneda-Paz JL, Borevitz JO, Ecker JR, Kay SA. LUX ARRHYTHMO encodes a Myb domain protein essential for circadian rhythms. Proc Natl Acad Sci U S A. 2005 Jul 19; 102 (29):10387–92. https://doi.org/10.1073/pnas.0503029102 PMID: 16006522

88. Conn SJ, Hocking B, Dayod M, Xu B, Athman A, Henderson S, et al. Protocol: optimising hydroponic growth systems for nutritional and physiological analysis of Arabidopsis thaliana and other plants. Plant Methods. 2013 Feb 5; 9(1):4. https://doi.org/10.1186/1746-4811-9-4 PMID: 23379342

89. Litthauer S, Battle MW, Lawson T, Jones MA. Phototropins maintain robust circadian oscillation of PSII operating efficiency under blue light. Plant J. 2015 Sep; 83(6):1034–45. https://doi.org/10.1111/tpj.12947 PMID: 26215041

90. Rees H, Duncan S, Gould P, Wells R, Greenwood M, Brabbs T, et al. A high-throughput delayed fluorescence method reveals underlying differences in the control of circadian rhythms in Triticum aestivum and Brassica napus. Plant Methods. 2019 Dec 21; 15(1):51.

91. Zielinski T, Moore AM, Troup E, Halliday KJ, Millar AJ. Strengths and limitations of period estimation methods for circadian data. PLoS ONE. 2014; 9(5):e96462. https://doi.org/10.1371/journal.pone.0096462 PMID: 24809473

92. Johnson M, Frasier S. Nonlinear least squares analysis. Methods Enzym. 1985; 117:301–42.

93. Straume M, Frasier-Cadoret SG, Johnson ML. Least-Squares Analysis of Fluorescence Data. In: Topics in Fluorescence Spectroscopy. Boston: Kluwer Academic Publishers; 2002. p. 177–240.

94. Bresenham JE. Algorithm for computer control of a digital plotter. IBM Syst J. 1965; 4(1):25–30.

95. Wetzler A. Bresenham optimized for Matlab [Internet]. 2010 [cited 2017 Jan 10]. Available from: https://uk.mathworks.com/matlabcentral/fileexchange/28190-bresenham-optimized-for-matlab

96. Daubechies I. The wavelet transform, time-frequency localization and signal analysis. IEEE Trans Inf Theory. 1990; 36(5):961–1005.

97. Torrence C, Compo GP, Torrence C, Compo GP. A Practical Guide to Wavelet Analysis. Bull Am Meteorol Soc. 1998 Jan 1; 79(1):61–78.

98. Soroldoni D, Jörg DJ, Morelli LG, Richmond DL, Schindelin J, Jülicher F, et al. A Doppler effect in embryonic pattern formation. Science. 2014; 345(6193).

99. Webb AB, Lengyel IM, Jörg DJ, Valentin G, Jülicher F, Morelli LG, et al. Persistence, period and precision of autonomous cellular oscillators from the zebrafish segmentation clock. Elife. 2016 Feb 13; 5: e08438. https://doi.org/10.7554/eLife.08438 PMID: 26880542

100. Edwards KD, Akman OE, Knox K, Lumsden PJ, Thomson AW, Brown PE, et al. Quantitative analysis of regulatory flexibility under changing environmental conditions. Mol Syst Biol. 2010 Jan 1; 6(1):424.

101. Illustrations P. Root illustrations [Internet]. Database: figshare. 2018 [cited 2019 Mar 28]. Available from: https://figshare.com/collections/Root_illustrations/3701038